A model of optimal protein allocation during phototrophic growth

Marjan Faizi[a], Tomáš Zavřel[b], Cristina Loureiro[c], Jan Červený[b], Ralf Steuer[a,*]

[a] Humboldt-Universität zu Berlin, Institut für Biologie, Fachinstitut für Theoretische Biologie (ITB), 10115 Berlin, Germany
[b] Department of Adaptive Biotechnologies, Global Change Research Institute CAS, Brno, Czech Republic
[c] Department of Applied Physics, Polytechnic University of Valencia, Valencia, Spain

ARTICLE INFO

ABSTRACT

Photoautotrophic growth depends upon an optimal allocation of finite cellular resources to diverse intracellular processes. Commitment of a certain mass fraction of the proteome to a specific cellular function typically reduces the proteome available for other cellular functions. Here, we develop a semi-quantitative kinetic model of cyanobacterial phototrophic growth to describe such trade-offs of cellular protein allocation. The model is based on coarse-grained descriptions of key cellular processes, in particular carbon uptake, metabolism, photosynthesis, and protein translation. The model is parameterized using literature data and experimentally obtained growth curves. Of particular interest are the resulting cyanobacterial growth laws as fundamental characteristics of cellular growth. We show that the model gives rise to similar growth laws as observed for heterotrophic organisms, with several important differences due to the distinction between light energy and carbon uptake. We discuss recent experimental data supporting the model results and show that coarse-grained growth models have implications for our understanding of the limits of phototrophic growth and bridge a gap between molecular physiology and ecology.

1. Introduction

Phototrophic microorganisms, including cyanobacteria, are of significant interest as potential host organisms for the renewable synthesis of pharmaceuticals, food supplements, and chemical bulk products (Ducat et al., 2011; Wijffels et al., 2013; Zavřel et al., 2016). As the only known oxygen-evolving photoautotrophic prokaryotes, cyanobacteria possess several advantageous properties that make them promising candidates for biotechnological applications: cyanobacteria use sunlight, water, and atmospheric CO_2 as their primary source of energy, reducing power, and carbon, respectively. They thrive in almost all environments, from Antarctica to hot springs and deserts, as well as from fresh water to highly saline ecosystems (Oren, 2014). Cultivation is possible in salt and brackish water, thereby avoiding direct competition with conventional agriculture. Cyanobacteria are genetically tractable and exhibit high photoautotrophic growth rates.

The capability to grow with high rates in diverse environments, is frequently emphasized as a key requirement for applications in green biotechnology (Burnap, 2015; Yu et al., 2015; Bernstein et al.,

2016). Many cyanobacteria, including well-characterized model strains, have typical doubling times of 7–12 h or more (Bernstein et al., 2016; Burnap, 2015). The fastest reported doubling time of a cyanobacterium to date is 1.9 h (Yu et al., 2015). Given the importance of fast growth as an indicator of overall culture productivity, however, the (molecular) limits of phototrophic growth are still insufficiently understood. Only recently, a number of computational (Burnap, 2015; Rügen et al., 2015; Mueller et al., 2017; Reimers et al., 2017), as well as experimental (Bernstein et al., 2016; Yu et al., 2015; Abernathy et al., 2017) studies have begun to investigate the molecular limits of phototrophic growth.

In this work, we develop a small-scale kinetic model of cyanobacterial phototrophic growth based on a coarse-grained description of relevant intracellular processes. Using the computational model, we seek to understand the organization of phototrophic growth in terms of the cellular 'protein economy' (Molenaar et al., 2009; Burnap, 2015; Rügen et al., 2015; Reimers et al., 2017) of growth. That is, we seek to understand how a growing cell may optimally allocate its limited energy and protein resources to different intracellular processes relevant for phototrophic growth, including protein translation, photosynthetic electron transport, carbon uptake and metabolism.

Our approach is based on similar models already available for heterotrophic growth. Since the seminal studies of Jacques Monod

describing the growth of a bacterial culture (Monod, 1949), a wealth of information has been acquired with respect to the physiology of growing bacterial cells (Schaechter, 2015; Neidhardt, 1999). Of particular interest are fundamental characteristics of growth that are independent of the chemical nature of the medium, such as the gross chemical composition in terms of protein, RNA, DNA, carbohydrates and lipids (Neidhardt, 1999). An early key observation was that several of these characteristics are simple monotonic functions of growth rate (Marr, 1991; Neidhardt, 1999) – in particular the concentration of ribosomes was found to be a linear function of growth rate (Ecker and Schaechter, 1963).

Since then, a number of experimental and theoretical studies have addressed the covariation between the cellular composition of macromolecules and the growth rate for heterotrophic microorganisms (Marr, 1991; Klumpp et al., 2009; Scott et al., 2010; Bosdriesz et al., 2015). These models are either large-scale constraint-based models, such as models described by resource balance analysis (Goelzer et al., 2015; Goelzer and Fromion, 2017) and related time-dependent approaches (Rügen et al., 2015; Reimers et al., 2017), or small-scale kinetic models that describe fundamental processes of cellular growth by coarse-graining the proteome into few essential classes (Molenaar et al., 2009; Maitra and Dill, 2015; Weiße et al., 2015). Properties of the respective models are typically evaluated in the context of evolutionary *optimality*: the allocation of proteins to the respective processes is assumed to be optimal in the sense that the growth rate in a given environment is maximal, and that synthesizing more protein within one class, at the expense of other classes, would lower the overall growth rate (Marr, 1991). While there are certainly caveats concerning the assumption of optimality, the application of optimization methods has a long tradition in the study of metabolic systems (Heinrich and Schuster, 1996) and represents a useful starting point to investigate and benchmark protein allocation in growing cells (Klipp et al., 2002; Gottstein et al., 2014; Müller et al., 2015).

While several large- and medium-scale constraint-based models that consider resource allocation during phototrophic growth have been proposed (Rügen et al., 2015; Reimers et al., 2017), to the best of our knowledge, as yet only a single study considered phototrophic resource allocation from the perspective of a coarse-grained kinetic model (Burnap, 2015). Here, we therefore develop such a model, based on ordinary differential equations (ODEs), that allows us to describe the optimality of the macromolecule composition for cyanobacterial balanced growth under different environmental conditions. Our model is based on recent resource allocation models for heterotrophic growth, in particular the models of Molenaar et al. (2009), Maitra and Dill (2015) and Weiße et al. (2015), but accounts for the specific properties of photoautotrophic growth. Going beyond the study of Burnap (2015), we consider a primitive CO_2-concentrating mechanism and the consequences of photodamage on protein allocation. The model is parameterized using experimentally determined growth curves for the cyanobacterial strain *Synechocystis* sp. PCC 6803. Our key questions are: (i) does a coarse-grained model of cyanobacterial growth allow us to reproduce experimentally observed growth curves? (ii) does a model of phototrophic growth give rise to similar growth laws as observed for heterotrophic growth? (iii) how do potential photodamage and carbon cycling impact observed growth laws, and (iv) what are the implications of growth models for biotechnology, ecology and our understanding of the limits of phototrophic growth?

2. A model of phototrophic growth

To describe cyanobacterial phototrophic growth, the relevant cellular processes are coarse-grained into three cellular functions:

(i) a minimal carbon metabolism consisting of carbon uptake and anabolic reactions, (ii) photosynthesis that provides cellular energy (and reducing power), and (iii) protein translation. The proteome is represented by four different protein classes: transporters (*T*) that facilitate uptake of inorganic carbon, metabolic enzymes (*M*) that catalyze carbon assimilation and anabolic reactions, ribosomes (*R*) that facilitate protein translation, and photosynthetic proteins (*P*) that produce cellular energy. The model structure is shown in Fig. 1.

The model consists of 7 ordinary differential equations (ODEs) that describe the dynamics of all internal compounds in units of numbers of molecules per cell. For simplicity, and following Weiße et al. (2015), we assume that the average cell volume is constant. In the initial model, we do not consider passive uptake or loss of inorganic carbon (carbon cycling) and damage induced by excessive light (photoinhibition). In the following, we briefly outline core components of the model, the full system of ODEs is provided in the supplementary text (Sections 1 and 2).

2.1. Carbon assimilation and metabolism

Uptake of inorganic carbon and its assembly into a (generic) amino acid *aa* is described in two steps: external inorganic carbon c_i^x is irreversibly imported (reaction v_t), facilitated by the transporter protein *T*, subsequently, intracellular inorganic carbon c_i is assimilated into organic carbon and converted into the amino acid *aa* (reaction v_m). The reaction v_m is catalyzed by a metabolic protein *M*, which represents all enzymes required to catalyze the conversion from c_i to *aa*. For simplicity, we do not distinguish between CO_2 and bicarbonate (HCO_3^-). The initial model does not include loss of intracellular inorganic carbon by passive diffusion (carbon cycling). The abundance of intracellular inorganic carbon c_i is governed by the differential equation

$$\frac{d[c_i]}{dt} = v_t - m_c \cdot v_m - \mu \cdot [c_i], \tag{1}$$

where m_c denotes the number of inorganic carbon molecules c_i required to produce one amino acid. The last term describes dilution by cellular growth, with μ denoting the growth rate. Both reaction rates are assumed to follow irreversible Michaelis–Menten kinetics and depend on the abundance of the energy unit *e*,

$$v_t = k_{cat}^t \cdot [T] \cdot \frac{[c_i^x]}{K_t + [c_i^x]} \cdot \frac{[e]}{K_e + [e]} \tag{2}$$

and

$$v_m = k_{cat}^m \cdot [M] \cdot \frac{[c_i]}{K_m + [c_i]} \cdot \frac{[e]}{K_e + [e]}, \tag{3}$$

where k_{cat}^t and k_{cat}^m denote the maximal turnover rates of the transporter and metabolic proteins, and K_t and K_m denote the corresponding half-saturation constants. The half-saturation constant K_m of the metabolic protein is set to mimic the low (relative) affinity of the enzyme ribulose-1,5-bisphosphate-carboxylase/-oxygenase (RuBisCO) for its substrate CO_2. For simplicity, the half-saturation constant K_e is assumed to be identical for all energy-dependent reactions. See Section 2.5 for model parameterization.

2.2. Ribosomes and protein translation

Protein translation is described analogous to earlier models for heterotrophic growth (Molenaar et al., 2009; Maitra and Dill, 2015; Weiße et al., 2015). Different from Weiße et al. (2015), we do not explicitly represent transcription and synthesis of mRNA. Protein complexes are translated by ribosomes *R*, using the precursor *aa*
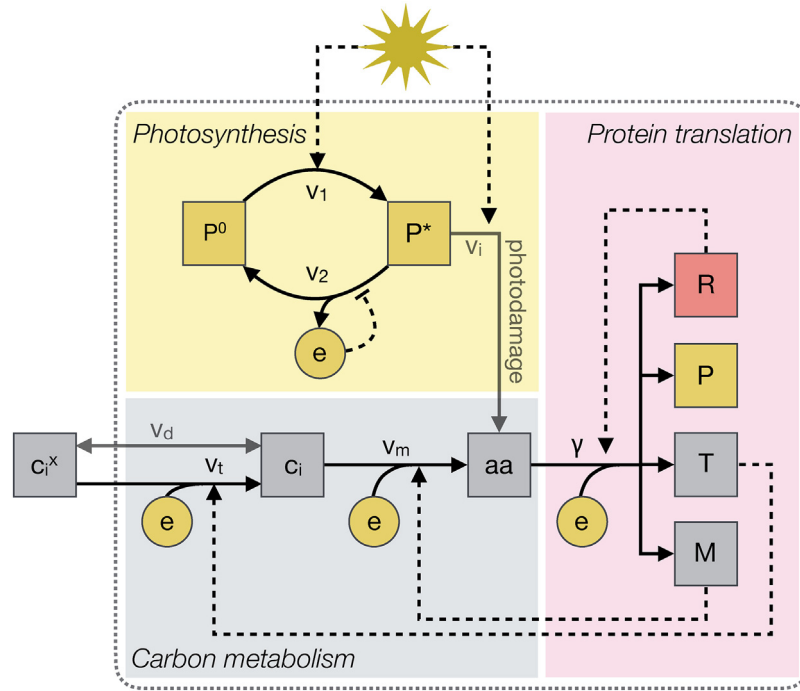
Fig. 1. A model of phototrophic growth. External inorganic carbon c_i^x is actively imported into the cell via a transporter $T (v_t)$. The metabolic enzyme M converts intracellular inorganic carbon molecules c_i into amino acids aa (v_m), the precursors for growth. Protein synthesis (γ) is facilitated by ribosomes R. All reactions depend on a cellular energy source, denoted as e. Cellular energy is obtained by the photosynthetic light reactions. The photosynthetic unit P exists in two states: active (P^*) and inactive (P^0). P^0 is activated by light absorption (v_1), and energy is released during the transition between the activated to the inactivated state (v_2). The latter reaction is subject to product inhibition. The model is later extended to account for photodamage (v_i), as well as for uptake (and loss) of inorganic carbon by passive diffusion (v_d).

and energy. The translation rate γ_j of a protein complex j with a length of n_j (in units of amino acids) is

$$\gamma_j = \beta_j \cdot [R] \cdot \frac{\gamma_{\max}}{n_j} \cdot \frac{[e]}{K_e + [e]} \cdot \frac{[aa]}{K_a + [aa]}, \tag{4}$$

where $\gamma_{\max}$ denotes the maximal elongation rate that is divided by the size of the protein complex n_j to account for the fact that larger complexes take longer to translate (Weiße et al., 2015). The parameter K_a denotes the half-saturation constant of ribosomes for amino acids and the factor β_j denotes the fraction of total ribosomes allocated to the translation of protein complex j. The factors β_j therefore determine the allocation of resources to cellular functions and fulfill the constraint

$$\sum_{j \in \mathcal{P}} \beta_j \leq 1, \quad \forall j : \beta_j \geq 0, \tag{5}$$

with $\mathcal{P} = \{R, P, T, M\}$. The dynamics of the abundance of each protein complex is given by the difference between translation rate and dilution by cell growth. For example, the amount of ribosomes is governed by the following differential equation (and analogously for all other protein complexes)

$$\frac{d[R]}{dt} = \gamma_R - \mu \cdot [R]. \tag{6}$$

We assume that for fast growing cells, protein degradation is negligible compared to the dilution term describing cell growth (with the exception of photodamage discussed below).

2.3. Photosynthesis and the electron transport chain

The conversion of light into cellular energy is described analogously to existing three-state models of phototrophic growth (Megard et al., 1984; Eilers and Peeter, 1988; Zonneveld, 1997). Specifically, we follow the model of Han (2001) and describe light harvesting and the electron transport chain as a single process that

is facilitated by a photosynthetic unit P. The photosynthetic unit is defined as the assembly of light-harvesting complexes, photosystems II and I, and the photosynthetic electron transport chain (Han, 2001). The photosynthetic unit P exists in two states: inactivated P^0 and activated P^*. Absorption of light facilitates the transition to the activated state P^* (reaction v_1 in Fig. 1). The transition from the activated state P^* to the inactivated state P^0 then results in the production of a cellular energy unit e (reaction v_2 in Fig. 1). For simplicity, we do not distinguish between reducing power and chemical energy (ATP): the energy unit e is understood as an abstract entity that combines contributions from ATP, GTP and NADPH.

The photosynthetic cycle is assumed to be fast, compared to the timescales of translation. We obtain an expression that describes the reaction rate v_2 in terms of total photosynthetic unit $[P] = [P^0] + [P^*]$,

$$v_2 = \frac{k_2(e) \cdot \hat{\sigma} \cdot I \cdot [P]}{\hat{\sigma} \cdot I + k_2(e) + \mu}, \tag{7}$$

where $k_2(e)$ denotes the effective maximal turnover rate of the photosynthetic unit, subject to product inhibition exerted by the energy unit e. Light absorption is given by the product of the light intensity I and the effective absorption cross-section $\hat{\sigma}$ per photosynthetic unit. We note the two limiting regimes for the photosynthetic light reactions are: for high light ($\lim I \to \infty$), the rate approaches $v_2 = k_2(e) \cdot [P]$, thus the rate is only dependent on the amount of P per cell; for low light ($\hat{\sigma} \cdot I \ll k_2(e)$), and hence slow growth ($\mu \ll 1$), the rate approaches $v_2 = \hat{\sigma} \cdot I \cdot [P]$ and depends linearly on the absorbed light energy. We assume that per cycle m_ϕ units of e are released, hence the total synthesis rate of e is $m_\phi \cdot v_2$. Likewise, we assume that the release of molecular oxygen O_2 is proportional to v_2.

2.4. Describing cellular growth

The aim of our study is to investigate (balanced) cellular growth as a function of protein allocation expressed by the factors β_j. To this end, we require an expression of the specific growth rate μ as a function of kinetic parameters. Following Weiße et al. (2015), we consider the (average) cellular density $\mathcal{D}_c$ (or mass per volume) to be constant under different growth conditions and for different rates – a fact that is supported by experimental observations (Bremer and Dennis, 2008). The cellular density $\mathcal{D}_c$ is proportional to the weighted sum of the abundances of cellular components (the mass of components is measured in units of aa)

$$\mathcal{D}_c = \frac{[c_i]}{m_c} + [aa] + \sum_{j \in \mathcal{P}} n_j \cdot [j], \qquad (8)$$

with $\mathcal{P} = \{R, P, T, M\}$. Applying the steady-state assumption on the expression for $\mathcal{D}_c$ (see also supplementary text, section 2.4), we obtain an expression for the specific growth rate μ,

$$\mu = \frac{1}{\mathcal{D}_c} \frac{v_t}{m_c}. \qquad (9)$$

In the following, Eq. (9) serves as the objective function for the optimization problem. We seek to maximize μ as a function of protein allocation, as determined by the factors β_j (the allocation of translational capacity), subject to the constraint specified in Eq. (5). The formal optimization problem is defined in Section 6.2.

2.5. Parameterizing the model

We aim for a semi-quantitative model. That is, all relevant parameters should be within reasonable ranges and have a sound justification based on the biochemical literature. Model results, however, are understood as approximations, suitable to investigate general properties of phototrophic growth. Kinetic parameters were sourced from the literature and are summarized in Table 1.

Protein lengths (in units of aa) for the macromolecules R, P, and T were derived using the known molecular composition of macromolecules involved in the respective processes. The respective tables are provided in the supplementary text, Tables T2–T9. For the metabolic protein M, participating proteins were derived from the metabolic reconstruction of Knoop et al. (2013). Stoichiometric coefficients were approximated as follows: translation is assumed to require 3 energy units (one ATP and two GTP) per amino acid, each photosynthetic cycle results in 8 energy units (joint contributions from ATP and NADPH), and the amount of energy units required to synthesize one generic amino acid aa was approximated using the reconstruction of Knoop et al. (2013). The average cell density $\mathcal{D}_c$ (protein mass per cell in units of aa) is calculated by assuming that the mass fraction of proteins considered in the model is $\approx 25\%$ of the cell dry weight (we assume that the total proteome is about 50% of cell dry weight). We do not consider constituent proteins and other cellular components explicitly. Cell surface and volume (A_{cell} and V_{cell}) are calculated by assuming a spherical shape with an average cell radius of $1.75\,\mu m$ (for derivation of the cell radius see supplementary text, section 3.3).

We consider the enzyme ribulose-1,5-bisphosphate-carboxylase/-oxygenase (RuBisCO) as the rate-limiting step in metabolism. Its affinity $K_m = 181\,\mu M$ (Marcus et al., 2005) is converted into molecules per cell using the conversion factor $1\,\mu M = 10^{-6} \cdot N_A \cdot V_{cell}$ [molecs cell^{-1}]. Remaining intracellular half-saturation constants (K_a, K_e) are set to low arbitrary values. The synthesis of the energy unit e is subject to product inhibition using an (arbitrarily set) inhibition constant K_i to prevent unreasonable accumulation of e.
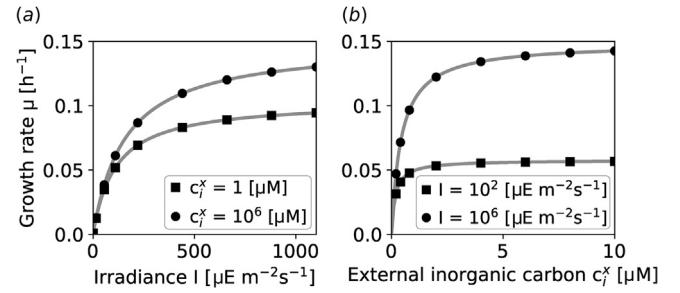
Fig. 2. The model reproduces Monod-like growth curves. Maximal growth rates (black circles and squares) are determined by optimizing protein allocation for different values of light intensity I and external inorganic carbon c_i^x. Solid gray lines indicate the two-substrate Monod equation (11) fitted to the model-derived growth rates.

The remaining unknown parameters are the effective absorption cross-section $\hat{\sigma}$ of P, the photodamage rate k_d, as well as the maximal turnover rate of the photosynthetic unit τ, given by

$$k_2(e) = \frac{\tau}{1 + \left(\frac{[e]}{K_i}\right)^4}. \qquad (10)$$

These parameters ($\hat{\sigma}$, k_d, τ) are estimated using experimentally obtained growth curves for *Synechocystis* sp. PCC 6803 under CO_2-saturating conditions (see Section 4.3). The fit was obtained using a reference concentration of external inorganic carbon $c_i^x = 1000\,\mu M$. For the initial model the fitted parameters were used, with k_d and P_m equal to zero (neglecting diffusion and photodamage). Details about the estimated and fitted parameters are provided in the supplementary text (section 3).

3. The protein economy of phototrophic growth

We seek to evaluate the model with respect to bacterial growth laws. To this end, we vary the proteome allocation, as determined by the factors β_j, to maximize the growth rate μ, specified in Eq. (9). All computations were carried out in *Python 2.7* using the package *scipy.optimize*. Parameters are as specified in Table 1, except otherwise noted.

3.1. Growth kinetics of the model

We solve the optimization problem as a function of the concentration of external inorganic carbon $[c_i^x]$ and light intensity I. The resulting growth curves, shown in Fig. 2, are consistent with the Monod equation. Similar results have been obtained for heterotrophic bacteria (Molenaar et al., 2009; Weiße et al., 2015). The Monod curves allow to estimate the (model-based) maximal growth rate μ^{max} under saturating concentrations of external inorganic carbon and light. The resulting value $\mu^{max} = 0.149\,h^{-1}$ corresponds to a doubling time of approximately 4.65 h, well within a reasonable range for the growth rate of *Synechocystis* sp. PCC 6803, and slightly slower than the fastest reporting doubling times for cyanobacteria (Yu et al., 2015; Bernstein et al., 2016).

Considering the co-limitation by external inorganic carbon $[c_i^x]$ and light availability I (Saito et al., 2008), the growth curve is not consistent with a multiplicative dual-substrate Monod equation. Neither is the growth curve consistent with Liebig's law of the minimum where only one nutrient is the limiting nutrient. However, a Lineweaver–Burk plot (see supplementary text, Fig. S3) of growth rate versus light intensity for different inorganic carbon concentrations shows parallel lines, which is indicative of uncompetitive inhibition. Therefore, we conjecture that the growth law is consis-

USE MENTEN COSTANTS FOR INITIAL CONCENTRATION VALUES FOR VARIABLES

Table 1
Parameters of the model. Parameters mainly relate to the cyanobacterial species *Synechocystis* sp. PCC 6803• (and *Synechococcus* sp. strain PCC 7942∘). If no data were available in the literature, parameters are adopted from *E. coli*∗. The remaining parameters are estimated here◇ or fitted□ (see supplementary text, Section 3.3). Amino acids are abbreviated as *aa* and molecules as *molecs* for the units.

Parameter	Definition	Value	Source
P_m	Cell membrane permeability to c_i^x	0.0018 (dm min^{-1})	Mangan and Brenner (2014)
A_{cell}	Cell surface area	3.85×10^{-9} (dm^2 cell^{-1})	◇
V_{cell}	Cell volume	2.24×10^{-14} (L cell^{-1})	◇
N_A	Avogadro constant	6.022×10^{23} (mol^{-1})	
k_{cat}^t	Maximal import rate	726 (min^{-1})	Dornmair et al. (1989) ∗
K_t	Half-saturation constant of T	15 (μM)	Omata et al. (2002) ∘
k_{cat}^m	Maximal metabolic rate	545 (min^{-1})	Marcus et al. (2005) •
K_m	Half-saturation constant of M	2441560 (molecs cell^{-1})	Marcus et al. (2005) •
γ_{max}	Maximal translation rate	1320 (aa min^{-1} molecs^{-1})	Bremer and Dennis (2008) ∗
K_a, K_e	Half-saturation constants for e and aa	10000 (molecs cell^{-1})	◇
$\hat{\sigma}$	Effective absorption cross-section of P	0.166 (m^2 μE^{-1})	□
τ	Maximal turnover rate of P	1900 (min^{-1})	□
k_d	Rate constant for photodamage	1.6×10^{-6}	□
K_i	Product-inhibition constant for e synthesis	10^8 (molecs cell^{-1})	◇
$\mathcal{D}_c$	Average density (protein mass per cell)	1.4×10^{10} (aa cell^{-1})	•
n_R	Ribosome length	7358 (aa molecs^{-1})	•
n_T	Transporter length	1681 (aa molecs^{-1})	•
n_M	Length of metabolic enzyme complex	28630 (aa molecs^{-1})	•
n_P	Length of photosynthetic unit	95451 (aa molecs^{-1})	•
m_μ	Amount of e consumed to create one aa	45	•
m_γ	Amount of e needed for one transl. elong. step	3	•
m_ϕ	Amount of e produced by P cycle	8	•
m_c	Average carbon chain length of an aa	5	•

tent with a rate equation in which absence of a nutrient corresponds to (uncompetitive) inhibition,

$$\mu = \frac{\mu^{\max} \cdot I/K_I^x \cdot [c_i^x]/K_c^x}{I/K_I^x + [c_i^x]/K_c^x + (I \cdot [c_i^x])/(K_I^x \cdot K_c^x)}. \tag{11}$$

Using Eq. (11), we obtain the effective half-saturation constants for the external nutrients, $K_I^{eff} = 158\,\mu$E m^{-2} s^{-1} and $K_c^{eff} = 0.43\,\mu$M, respectively. The half-saturation constant for external inorganic carbon is significantly below the corresponding half-saturation constants for the transporter and metabolic reaction ($K_t = 15\,\mu$M and $K_m = 181\,\mu$M, see Section 2.5). The decrease of the effective half-saturation constant for external inorganic carbon indicates that the irreversible transport implements a rudimentary carbon concentrating mechanism (CCM). We observe that for the optimized solution, the intracellular concentration is at all times sufficient to saturate the metabolic enzyme M. Likewise, the intracellular concentration of the energy unit e is at all times sufficient to saturate all energy consuming reactions. Saturation of reactions with their respective substrates ensures that intracellular reactions, including protein translation, operate close to their maximal capacities.

3.2. Protein allocation and phototrophic growth laws

As the next step, we study protein allocation, optimized for maximal growth rate, as a function of environmental conditions. Fig. 3 shows the model-derived optimal protein allocation for phototrophic growth. Using light intensity I and external inorganic carbon c_i^x as parameters, the factors β_j were optimized to give rise to a maximal growth rate μ. Corresponding to results obtained for earlier models of heterotrophic growth, the ribosomal mass fraction is a linear function of the growth rate, irrespective of whether I and c_i^x is changed. Indeed, the linear dependence is a direct consequence of the model definitions. Re-arranging Eq. (6) and assuming that translation is saturated with respect to its substrates aa and e, we obtain

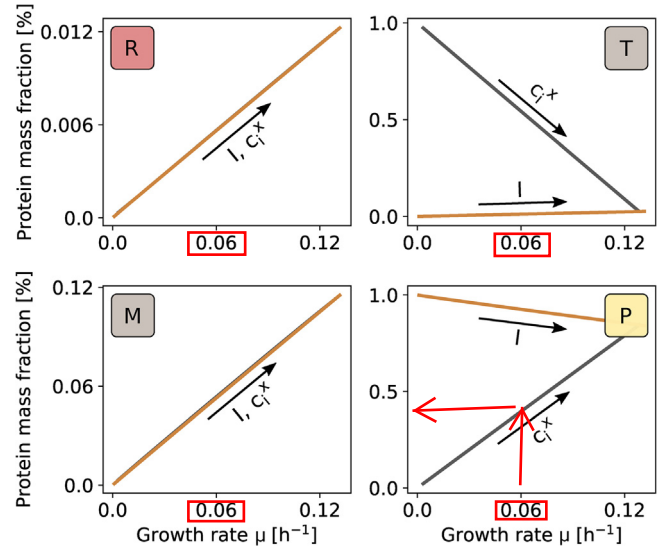$$\mu = \beta_R \cdot \frac{\gamma_{\max}}{n_R}, \tag{12}$$

Fig. 3. Protein allocation and phototrophic growth laws. Protein mass fractions are linearly dependent on the growth rate. Optimal protein mass fractions are calculated for increasing light intensity I and fixed external inorganic carbon $c_i^x = 1000\,\mu$M, as well as for increasing external inorganic carbon c_i^x and fixed light intensity $I = 1000\,\mu$E m^{-2}s^{-1}. The mass fraction of ribosomal and metabolic proteins (R, M) linearly increases with increasing growth rate, irrespective of whether growth is enhanced by increasing c_i^x or I. The mass fraction of the transporter protein (T), however, decreases linearly with increasing carbon availability, whereas it increases for increasing light availability. Vice versa, the mass fraction of the photosynthetic unit (P) decreases linearly with increasing light intensity and increases for increasing carbon availability.

whereby β_R corresponds to the amount of ribosomes allocated to their own synthesis.

All other protein fractions likewise exhibit a linear relationship with respect to the growth rate. The amount of metabolic enzyme M, relative to total protein, is linearly increasing with growth rate, irrespective of whether the increase in growth is caused by increasing external inorganic carbon or increasing light

intensity. In contrast, the relative mass fraction of the transporter T decreases with increasing external inorganic carbon, and increases with increasing light intensity. The former, a decrease of transporter with increasing availability of the carbon source, was also observed in the (heterotrophic) model of Molenaar et al. (2009). Specific for phototrophic organisms, the mass fraction of the photosynthetic unit P decreases with increasing light intensity and increases with increasing external inorganic carbon. The former agrees with the numerical result of Burnap (2015) where the mass fraction of the light-harvesting complex (LHC) decreases with increasing light intensity. Similar, for steady-state day metabolism, the large-scale model of Reimers et al. (2017) predicted an increase in the number of ribosomes with increasing growth rate due to an increasing light intensity, as well as a decrease in the number of photosystems with increasing light intensity.

Our results show that the bacterial growth laws, previously determined mostly for heterotrophic organisms, hold also for models of phototrophic growth where the carbon and energy source are separate. The observed growth rates are also in good agreement with results obtained from large-scale constraint-based models. In the following, we extend the model to incorporate aspects of photodamage and carbon cycling.

4. Extending the initial model: photodamage and carbon cycling

4.1. High light intensities and photodamage

As yet, the model did not account for two hallmark properties of cyanobacterial phototrophic growth, potential photodamage and carbon cycling. Light absorption damages the photosynthesis machinery proportional to the light intensity (Tyystjärvi, 2008). The resulting photodamage has significant impact on the observed growth curve. A number of (mainly phenomenological) minimal models reproduce the decrease in growth rate under high light. In particular, three state models of the photosynthesis-irradiance (PI) curve typically reproduce the inhibitory effect of high light intensities (Han, 2002). See Westermark and Steuer (2016) for a recent review.

To account for potential photodamage, we follow Han (2002) and assume that the active state of the photosynthetic unit P^* can be irreversibly damaged by further light absorption. The protein is then degraded into amino acids aa, mimicking the repair-cycle of the D1 subunit (Tyystjärvi, 2008). The rate of damage (v_i) is assumed to be a linear function of light intensity,

$$v_i = k_d \cdot \hat{\sigma} \cdot I \cdot [P^*], \tag{13}$$

where k_d denotes the first-order rate constant. The inclusion of photodamage modifies the dynamics of the total photosynthetic unit P,

$$\frac{d[P]}{dt} = \gamma_P - v_i - \mu \cdot [P], \tag{14}$$

as well as the quasi-steady state expression for the photosynthetic capacity, Eq. (7),

$$v_2 = \frac{k_2(e) \cdot \hat{\sigma} \cdot I \cdot [P]}{\hat{\sigma} \cdot I + k_2(e) + k_d \cdot \hat{\sigma} \cdot I + \mu}. \tag{15}$$

See the supplementary text for the complete set of ODEs. The only additional kinetic parameter is the first-order rate constant k_d. Its value is estimated using experimentally determined growth curves (see Section 4.3).

4.2. Diffusion and carbon cycling

In addition to potential photodamage, we account for the fact that some forms of inorganic carbon, in particular CO_2, are permeable. Diffusion of inorganic carbon via the cell membrane results in two effects: at high concentrations of external inorganic carbon, passive diffusion is sufficient to meet the carbon requirements of metabolism and active transport is not required. Vice versa, for low concentrations of external inorganic carbon and high activity of the transporter reaction, passive diffusion results in leakage of inorganic carbon from the cell. The inclusion of diffusion, together with the active transport mechanism, therefore implements a primitive inorganic carbon concentrating mechanism (CCM): to increase the concentration of intracellular carbon relative to the extracellular concentration, the transport reaction has to operate against a diffusion gradient.

To account for passive diffusion, we assume that the diffusion reaction (v_d) depends on the permeability of the cell membrane P_m, the cell surface A_{cell} and the gradient between internal and external c_i

$$v_d = P_m \cdot A_{cell} \cdot (N_A \cdot [c_i^x] - \frac{[c_i]}{V_{cell}}), \tag{16}$$

where V_{cell} and N_A are the cell volume and the Avogadro constant, respectively. For simplicity, A_{cell} and V_{cell} are assumed to be constant. The inclusion of the diffusion reaction results in a modified ODE for intracellular inorganic carbon, Eq. (1),

$$\frac{d[c_i]}{dt} = v_t + v_d - m_c \cdot v_m - \mu \cdot [c_i]. \tag{17}$$

Likewise, the expression for the growth rate, Eq. (9), is modified (see supplementary text, section 2.4),

$$\mu = \frac{1}{\mathcal{D}_c} \frac{v_t + v_d}{m_c}. \tag{18}$$

4.3. Comparison to experimental growth curves

The inclusion of photodamage and diffusion allows the model to reproduce the characteristic cyanobacterial growth curve. To this end, we measured the growth rate of *Synechocystis* sp. PCC 6803 in a turbidostat culture as a function of light intensity under increased CO_2, corresponding to carbon-saturated growth. See Materials and Methods for details. The experimental growth curve is shown in Fig. 4a. The data were used to fit three unknown parameters in the extended model, namely the turnover rate τ, the effective absorption cross-section $\hat{\sigma}$, and the rate constant of photodamage k_d. The model and the experimentally derived growth curve are in good agreement (Fig. 4a).

The fitted model can subsequently be used to predict the functional form of the oxygen evolution rate as a function of light intensity I. Since the model does not explicitly account for oxygen evolution, we approximate the oxygen evolution with the turnover of the photosynthetic unit (v_2). No further parameters were adjusted. The functional form of the model-derived turnover rate is in good agreement with the measured oxygen evolution (Fig. 4b).

4.4. Sensitivity analysis and the limits of growth

Using the fitted model, we seek to evaluate the impact of all model parameters, including the availability of external inorganic carbon and light intensity, on the growth rate (sensitivity analysis). To this end, we consider two scenarios: growth under saturating carbon conditions ($c_i^x = 1000\,\mu M$), as well as carbon-limited growth ($c_i^x = 50\,\mu M$). The results are shown in Fig. 5.
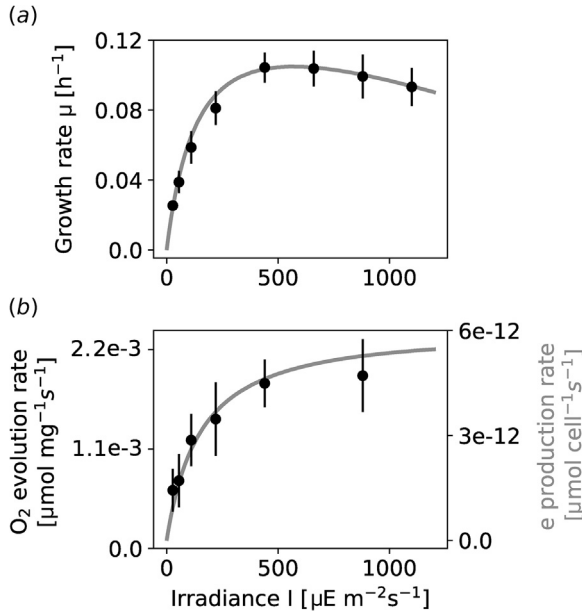
Fig. 4. The model reproduces experimental cyanobacterial growth curves. (a) The steady-state growth rate of *Synechocystis* sp. PCC 6803 (black circles) was measured experimentally in turbidostat culture for 8 different light intensities with 6–11 biological replicates each. Model simulations (solid gray line) were fitted (see Section 2.5) using a constant external inorganic carbon value of $c_i^x = 1000\,\mu M$ (growth under saturating carbon conditions). (b) The model was subsequently used to compare the model-derived photosynthetic turnover rate v_2 (gray line) to the photosynthetic oxygen evolution rate per dry weight. Both curves qualitatively agree (no further parameters were adjusted).

The (logarithmic) sensitivity coefficient (see Materials and Methods) describes the impact of a change in a parameter on the growth rate: a sensitivity coefficient close to unity implies an (approximately) linear dependence. Fig. 5b shows the sensitivity coefficient of growth with respect to external parameters I and c_i^x. The sensitivity coefficient with respect to intracellular parameters

is shown in Fig. 5c for three different growth phases: (I) The first growth phase is characterized by light limitation for both values of external inorganic carbon availability. The model parameter with the highest impact on the growth rate is the effective absorption cross-section $\hat{\sigma}$ that determines the amount of light absorbed per photosynthetic unit. (II) The second growth phase corresponds to the point where the highest growth rate is attained. In this case, the sensitivity with respect to light intensity is zero. The model parameter with the highest impact on the growth rate is the turnover rate of the photosynthetic unit τ. (III) The third growth phase is characterized by increasing photoinhibition, i.e., a light-induced reduction of growth rate. In this case, the model parameter with the highest impact on the growth rate is the turnover rate of the photosynthetic unit τ, whereas an increasing effective absorption cross-section $\hat{\sigma}$ has a negative impact on growth. An increase of the turnover rate τ minimizes the abundance of the photosynthetic unit in its activated state and hence reduces the impact of photoinhibition. Other model parameters, in particular the maximal elongation rate γ_{max}, have comparatively low impact on the estimated growth rate.

4.5. Effects of photodamage and diffusion on phototrophic growth laws

We are specifically interested in how the incorporation of photodamage and diffusion impacts the phototrophic growth laws shown in Fig. 3. Fig. 6 shows the modified growth laws for the extended model. We consider optimal protein allocation for increasing light intensity for two different amounts of extracellular inorganic carbon (Fig. 6a), as well as optimal protein allocation for increasing extracellular inorganic carbon for two different light intensities (Fig. 6b). The corresponding intracellular concentrations of cellular precursors are provided in the supplementary text, Figs. S6 and S7.

For increasing light intensity I (and fixed c_i^x) the ribosomal mass fraction first increases proportional to the growth rate. For high light intensities and fast growth, however, the ribosomal mass continues to increase even as the growth rate again decreases due to photoinhibition. A similar phenomenon is observed for *E. coli* when
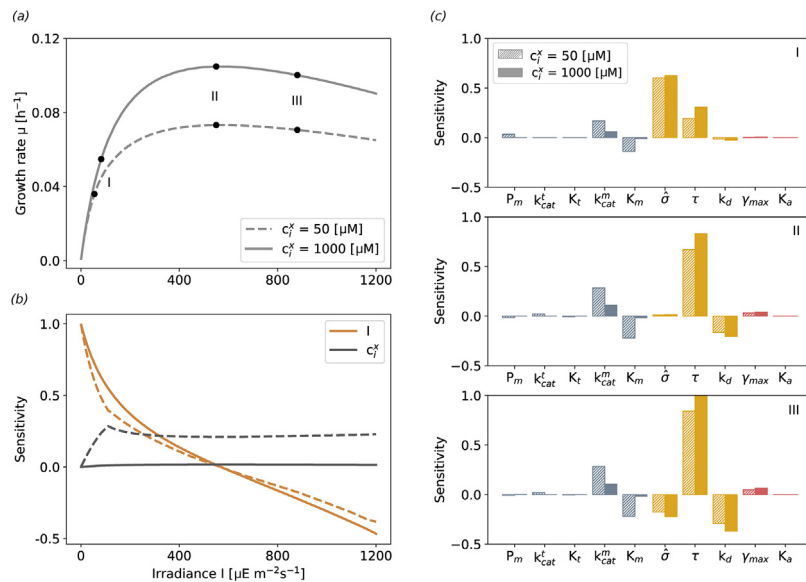

Fig. 5. Sensitivity analysis of the extended model with respect to environmental conditions and intracellular parameters. (a) Growth curves for two scenarios: carbon-saturating conditions ($c_i^x = 1000\,\mu M$, solid line), as well as carbon-limited conditions ($c_i^x = 50\,\mu M$, dashed line). (b) The (logarithmic) sensitivity with respect to external inorganic carbon c_i^x (gray line) and light intensity I (orange line). For low light, the sensitivity with respect to light intensity is close to unity, implying an (almost) linear dependence of growth as a function of light intensity. The sensitivity with respect to light then decreases until the maximal growth rate is attained. Subsequently, increasing light intensity has a negative impact on the growth rate (photoinhibition). The dependence on extracellular inorganic carbon differs between both growth scenarios. Under carbon-saturating conditions, the sensitivity remains close to zero for the entire growth curve. For low extracellular carbon, the sensitivity increases with increasing light intensity. (c) The sensitivity coefficients with respect to intracellular model parameters. The three growth phases correspond to the points marked in panel (a).
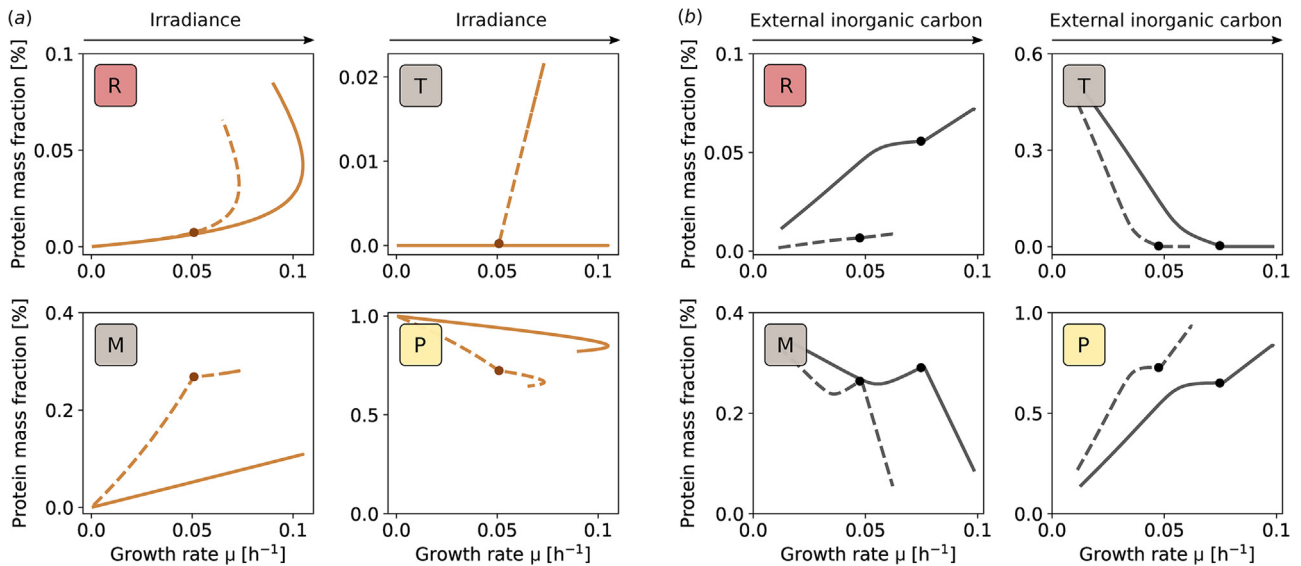
Fig. 6. Effects of photodamage and diffusion on phototrophic growth laws. (a) Protein mass fractions are displayed for increasing light intensity and fixed external inorganic carbon, $c_i^x = 50\,\mu M$ (dashed lines) and $c_i^x = 1000\,\mu M$ (solid lines). The solid circles indicate the transition point for which the transporter (T) mass fraction is more than 0.02%. (b) Protein mass fractions for increasing external inorganic carbon and fixed light intensities, $I = 100\,\mu E\,m^{-2}\,s^{-1}$ (dashed lines) and $I = 1000\,\mu E\,m^{-2}\,s^{-1}$ (solid lines). The solid circles indicate the transition point for which the transporter mass fraction is less than 0.3%.

nutrient amount is fixed and translational inhibitors are added to the medium (Scott et al., 2010): the cell compensates the inhibition of ribosomes by increasing the ribosomal mass fraction. In our case, the light-induced repair-cycle of the photosynthetic unit acts analogously to a translational inhibitor and requires to increase the ribosomal mass fraction. We note that, as a function of light intensity, the ribosomal mass fraction retains its linear dependence (see supplementary text, Fig. S7b).

For increasing light intensity I (and fixed c_i^x) the amount of transporter protein T exhibits a switch-like behavior. For high availability of external inorganic carbon ($c_i^x = 1000\,\mu M$), passive diffusion is sufficient to meet the carbon requirements of the cell and the transporter protein is not expressed. For low external inorganic carbon ($c_i^x = 50\,\mu M$), passive diffusion is only sufficient up to a critical threshold in the growth rate after which the transporter protein T is expressed (see supplementary text, Fig. S5). Conditional expression of bicarbonate transporter has been reported in the literature (McGinn et al., 2004; Burnap et al., 2015).

The remaining growth laws are qualitatively similar to the results shown in Fig. 3 – albeit with modifications to the simple linear relationships. In particular, the switch between passive diffusion and active transport, indicated with a dot in Fig. 6, induces shifts in the optimal protein allocation. Another noteworthy difference between the initial model and the extended model is the strong increase in the mass fraction of the metabolic protein M. Due to the inclusion of passive diffusion, the intracellular abundance of inorganic carbon is significantly lower in the extended model (up to two orders of magnitude). Due to the low affinity of the metabolic protein, the protein is not fully saturated for low external inorganic carbon – a fact that must be compensated by an increased mass fraction of the metabolic protein.

Overall, the results shown in Fig. 6 indicate that the growth laws for phototrophic growth are qualitatively retained when photodamage and diffusion are considered within the model – albeit with several important modifications. We conjecture that the actual protein mass fractions of phototrophic growth may be more complex than the simple linear dependencies hitherto described for heterotrophic growth.

5. Discussion and conclusions

Cyanobacteria are promising host organisms for green biotechnology. However, our current understanding of the molecular limits of cyanobacterial growth and the associated phototrophic growth laws is insufficient. Here, we developed a small-scale kinetic model of cyanobacterial phototrophic growth, based on ordinary differential equations, to describe optimal protein allocation under different environmental conditions. The model incorporates key processes related to phototrophic growth, i.e., carbon uptake, metabolism, photosynthesis and protein translation. Different from typical models of heterotrophic growth, we distinguish between two potentially limiting nutrients, external inorganic carbon and light.

The model was able to reproduce experimentally obtained phototrophic growth curves, including the inhibition of growth at high light intensities. The model also reproduced typical growth laws known from heterotrophic bacteria, in particular the fact that ribosomal mass fraction increases linearly with increasing growth rate (irrespective of whether the increase in growth rate is brought about by an increase in light intensity or an increase in availability of inorganic carbon). The growth laws obtained here are in good agreement with the effects of increasing light intensity on proteome allocation previously studied by Burnap (2015): the mass fraction of the photosynthetic unit (and hence light-harvesting complexes) decreases with increasing light intensity. Vice versa, the mass fraction of metabolic enzymes increases. Likewise, the growth laws exhibited by the coarse-grained model are in good agreement with the results observed for day metabolism in a recent large-scale constraint-based model of phototrophic growth (Reimers et al., 2017). We note that constraint-based models, such as the model of Reimers et al. (2017), typically involve several hundreds of reactions and require that all cellular interdependencies are formulated as a set of linear constraints. Such models are therefore complementary to the approach described here. The fact that both models exhibit similar growth laws indicates that the observed laws are robust with respect to model formulation.

Beyond a basic description of phototrophic growth, we also considered potential photodamage and diffusion. The extended model

gave rise to more complex phototrophic growth laws, while general properties and trends were preserved. In particular photodamage, mimicking the photoinhibition repair-cycle of enzymatic degradation and synthesis of the D1 protein, places an additional burden on ribosomal capacity – the resulting curves are similar to growth laws obtained for heterotrophic bacteria that are subject to a translational inhibitor. We conjecture, however, that the model, where photodamage primarily increases the requirement of translation, overestimates the effects of photodamage on the ribosomal mass fraction.

Compared to heterotrophic organisms, quantitative data on cyanobacterial growth laws under different growth conditions are still scarce. A few experimental studies have considered carbon and phosphorus allocation (MacKenzie et al., 2005; Raven, 2013), as well as rRNA contents (Binder and Liu, 1998; Worden and Binder, 2003). The latter point to a linear increase for intermediate growth rates, in good agreement with modeling results. The amount of rRNA per cell, however, plateaus or decreases at highest growth rates (explained at least in part by a decrease in cell size). Clarification would require direct measurements of cell size and protein content (Worden and Binder, 2003). Likewise, rRNA content is constant at lower growth rates (Worden and Binder, 2003). A similar deviation from model-derived optimality has already been observed for *E. coli* (Marr, 1991) – here, the higher relative amount of the ribosomal mass fraction at low growth rates is likely the result of an anticipatory adaptation to potential higher growth rates when nutrient availability increases.

The data that allow the most direct comparison with experimental protein allocation is the recent study of Bernstein et al. (2016). The authors measured the transcriptional responses to changing irradiance, and hence changing growth rate, in a turbidostat. Among the genes whose relative abundance of transcripts increases in direct proportion with growth rate were genes involved in translation (ribosomal proteins), amino acid biosynthesis and other genes involved in central carbon metabolism (Bernstein et al., 2016). Among the genes whose relative abundance of transcripts inversely correlates with growth rate were genes encoding photosystems I (PSI) and II (PSII) antenna proteins, as well as transcripts related to niche-adaptive protein functions (Bernstein et al., 2016). These results indicate similar trends as predicted here. For a detailed understanding of protein optimal allocation, however, further quantitative studies are needed. Computational models, such as the one presented here, will undoubtedly play an important role in interpreting such quantitative studies with respect to optimal adaptation of cyanobacteria to different growth conditions.

While our current small-scale model captures key properties of phototrophic growth, the model may be extended to address specific cellular functions in more detail. For example, currently, we only consider a minimal CCM and neglect photorespiration, as well as other photoprotective mechanisms. Future work may include the effects of cellular maintenance, basal respiration, and a more detailed representation of the electron transport chain. The latter will allow us to differentiate between the provision of energy and reductants, as well as between linear and cyclic electron transport – and thereby will allow us to make use of available data with respect to PSI/PSII ratio (Du et al., 2016). In future work, growth conditions may include fluctuating light to study energy dissipation and adaptation to varying light intensities. An ultimate goal is to improve our understanding of day/night regulation in diurnal environments, necessitating the inclusion of storage metabolism.

Finally, we also envision applications of this and similar small-scale growth models to bridge the gap between molecular physiology and ecology. It has recently been argued that future plankton models must place more emphasis on the underlying mechanisms of cell physiology, rather than on empirical parameter fitting (Allen and Polimene, 2011). To this date, the method of

choice for simulating resource-limited growth in ecological models remains the classic Monod equation (Monod, 1949), with only few advances to describe internal nutrient level (storage) and intracellular speciation (Hellweger, 2017). It has been emphasized that such models do not reflect the progress in our understanding of the underlying biological mechanisms, are disconnected from modern ecological problems (Hellweger, 2017), and do not allow for trade-offs between resource allocation and ecological dynamics as emergent properties (Allen and Polimene, 2011). We argue that models such as the one proposed here allow to relate growth properties to underlying molecular mechanisms. While still being numerically tractable, the complexity of coarse-grained growth models can be iteratively increased (Westermark and Steuer, 2016) – and therefore may serve as a suitable starting point to integrate ecophysiology with systems biology.

6. Materials and methods

6.1. Experimental procedures and growth data

As a reference organism, we used *Synechocystis* sp. PCC 6803, substrain GT-L (*Synechocystis* hereafter). *Synechocystis* was cultivated in a flat panel photobioreactor (Photon System Instruments, Brno, CZ) (Nedbal et al., 2008) under 27.5–1100 μmol photons m^{-2} s^{-1} of red light ($\lambda_{max} \approx 633$ nm, $\lambda_{1/2} \approx 20$ nm, Luxeon LXHLPD09, Future Lighting Solutions, Montreal, QC, Canada) supplemented with low portion of blue light (25 μmol photons m^{-2} s^{-1}, $\lambda_{max} \approx 445$ nm, $\lambda_{1/2} \approx 20$ nm, Luxeon LXHL-PR09; Future Lighting Solutions). The cultures were cultivated at 32 °C and the culture suspensions were bubbled by air supplemented with 0.5% CO_2 (v/v). The cultures were cultivated in a quasi-continuous regime operated as turbidostat according to Zavřel et al. (2015a). Briefly, the exponentially growing cultures were periodically diluted with fresh culture medium. The dilution was based on automatic measurements of culture optical density at 680 nm (OD_{680}); the OD_{680} range was set to 0.52–0.58 (approximately 10^7 cells ml^{-1}). The cultures were cultivated under each red light intensity for at least 24 h. This period was long enough to reach growth stability, i.e. to adapt to particular light conditions. After the growth stability was reached, samples were taken for measurement of cell count, cellular dry weight and concentration of chlorophyll a in the *Synechocystis* cells. Specific growth rates were calculated from changes in OD_{680} by applying an exponential regression model.

Dissolved oxygen was monitored by InPro6800 electrodes (Mettler-Toledo, Inc., Columbus, OH, USA). The oxygen evolution/respiration measurements were performed in the photobioreactor cuvette by turning off the cultures aeration for 10 min, through a 5 min light period and a 5 min dark period. Oxygen evolution/respiration rates were normalized per chlorophyll a content in *Synechocystis* cells, determined according to Zavrel et al. (2015b). The cell count was measured with a Cellometer Auto M10 (Nexcelom Bioscience, Lawrence, MA, USA). The cellular dry weight was measured with analytical balances XA105DR (Mettler-Toledo, Greifensee, CH).

6.2. Model implementation

The coarse-grained model is described by nonlinear rate equations and does not have an analytical solution, hence we are using numerical methods to solve the optimization problem. The optimization problem consists of finding the maximum specific growth rate μ (at steady-state) by varying the relative amount $\beta = \{\beta_R,$

$\beta_T, \beta_M, \beta_P\}$ of ribosomes that are allocated to translate a specific protein,

$$\max_\beta \quad \mu$$

$$\text{s.t.} \quad \sum_j \beta_j \leq 1, \tag{19}$$

$$\beta_j \geq 0, \quad \forall j \in \{R, T, M, P\}.$$

To obtain an estimate of the growth rate μ, we integrate the ODE system numerically until a steady-state is reached. The complete set of ODEs and their parameterization is provided in the supplementary text. The ODE system is implemented in Python 2.7 and available under the name *minimal_model.py*. To simulate the model results, we used the method *odeint* from the python package *scipy.integrate* for solving the ODEs and subsequently the method *minimize* from *scipy.optimize* for solving the optimization problem. The script to execute both steps is given in *simulate.py*.

6.3. Sensitivity analysis

The sensitivity is estimated for all model parameters and external conditions (I, c_i^x), except for the ribosome fractions (β). The (logarithmic) sensitivity s_i of the growth rate μ for a given parameter p_i is by the derivative

$$s_i = \frac{p_i}{\mu} \cdot \frac{d\mu(p_i)}{dp_i}, \tag{20}$$

and approximated by finite-size difference (0.1%) of a parameter in steady-state at the optimized growth rate. The value of the (logarithmic) sensitivity s_i corresponds to the kinetic order, i.e., a value close to one indicates a linear dependence of the growth rate on the parameter p_i.

Data accessibility. Python code of the model and for simulating the optimization results, as well as the experimental data, are given in the electronic supplementary material.

Author's contributions.

R.S. conceived of the study and designed the study.

M.F. carried out all computational simulations and drafted the manuscript.

T.Z., C.L., and J.C. carried out the growth experiments and carried out data analyses.

M.F. and R.S. wrote the manuscript.

All authors gave final approval for publication.

Conflict of interest

We declare that we have no conflict of interest.

Funding

Appendix A. Supplementary data

Supplementary data associated with this article can be found, in the online version, at https://doi.org/10.1016/j.biosystems.2018.02.004.

References

Abernathy, M.H., Yu, J., Ma, F., Liberton, M., Ungerer, J., Hollinshead, W.D., Gopalakrishnan, S., He, L., Maranas, C.D., Pakrasi, H.B., Allen, D.K., Tang, Y.J., 2017. Deciphering cyanobacterial phenotypes for fast photoautotrophic growth via isotopically nonstationary metabolic flux analysis. Biotechnol. Biofuels 10, 273.

Allen, J.I., Polimene, L., 2011. Linking physiology to ecology: towards a new generation of plankton models. J. Plankton Res. 33 (7), 989–997, http://dx.doi.org/10.1093/plankt/fbr032.

Bernstein, H.C., McClure, R.S., Hill, E.A., Markillie, L.M., Chrisler, W.B., Romine, M.F., McDermott, J.E., Posewitz, M.C., Bryant, D.A., Konopka, A.E., Fredrickson, J.K., Beliaev, A.S., 2016. Unlocking the constraints of cyanobacterial productivity: acclimations enabling ultrafast growth. mBio 7, http://dx.doi.org/10.1128/mBio.00949-16, ISSN 2150-7511.

Binder, B.J., Liu, Y.C., 1998. Growth rate regulation of rRNA content of a marine Synechococcus (cyanobacterium) strain. Appl. Environ. Microbiol. 64 (9), 3346–3351.

Bosdriesz, E., Molenaar, D., Teusink, B., Bruggeman, F.J., 2015. How fast-growing bacteria robustly tune their ribosome concentration to approximate growth-rate maximization. FEBS J. 282, 2029–2044, http://dx.doi.org/10.1111/febs.13258.

Bremer, H., Dennis, P.P., 2008. Modulation of chemical composition and other parameters of the cell at different exponential growth rates. EcoSal Plus 3 (1), http://dx.doi.org/10.1128/ecosal.5.2.3.

Burnap, R.L., Hagemann, M., Kaplan, A., 2015. Regulation of CO_2 concentrating mechanism in cyanobacteria. Life (Basel) 5, 348–371, http://dx.doi.org/10.3390/life5010348, ISSN 2075-1729.

Burnap, R.L., 2015. Systems and photosystems: cellular limits of autotrophic productivity in cyanobacteria. Front. Bioeng. Biotechnol. 3, 1, http://dx.doi.org/10.3389/fbioe.2015.00001.

Dornmair, K., Overath, P., Jähnig, F., 1989. Fast measurement of galactoside transport by lactose permease. J. Biol. Chem. 26 (1), 342–346.

Du, W., Jongbloets, J.A., Hernández, H.P., Bruggeman, F.J., Hellingwerf, K.J., dos Santos, F.B., 2016. Photonfluxostat: a method for light-limited batch cultivation of cyanobacteria at different, yet constant, growth rates. Algal Res. 20, 118–125, http://dx.doi.org/10.1016/j.algal.2016.10.004, ISSN 2211-9264, http://www.sciencedirect.com/science/article/pii/S2211926416304908.

Ducat, D.C., Way, J.C., Silver, P.A., 2011. Engineering cyanobacteria to generate high-value products. Trends Biotechnol. 29 (2), 95–103, http://dx.doi.org/10.1016/j.tibtech.2010.12.003.

Ecker, R.E., Schaechter, M., 1963. Ribosome content and the rate of growth of Salmonella typhimurium. Biochim. Biophys. Acta 76, 275–279, http://dx.doi.org/10.1016/0926-6550(63)90040-9, ISSN 0006-3002.

Eilers, P.H.C., Peeter, J.C.H., 1988. A model for the relationship between light intensity and the rate of photosynthesis in phytoplankton. Ecol. Model. 42 (3-4), 199–215, http://dx.doi.org/10.1016/0304-3800(88)90057-9.

Goelzer, A., Fromion, V., 2017. Resource allocation in living organisms. Biochem. Soc. Trans. 45 (4), 945–952, 08.

Goelzer, A., Muntel, J., Chubukov, V., Jules, M., Prestel, E., Nolker, R., Mariadassou, M., Aymerich, S., Hecker, M., Noirot, P., Becher, D., Fromion, V., 2015. Quantitative prediction of genome-wide resource allocation in bacteria. Metab. Eng. 32, 232–243.

Gottstein, W., Muller, S., Herzel, H., Steuer, R., 2014. Elucidating the adaptation and temporal coordination of metabolic pathways using in-silico evolution. BioSystems 117, 68–76.

Han, B.-P., 2001. Photosynthesis-irradiance response at physiological level: a mechanistic model. J. Theor. Biol. 213 (2), 121–127, http://dx.doi.org/10.1006/jtbi.2001.2413.

Han, B.-P., 2002. A mechanistic model of algal photoinhibition induced by photodamage to photosystem-II. J. Theor. Biol. 214 (4), 519–527, http://dx.doi.org/10.1006/jtbi.2001.2468.

Heinrich, R., Schuster, S., 1996. The Regulation of Cellular Systems. Chapman & Hall, New York, ISBN 0-412-03261-9.

Hellweger, F., 2017. 75 years since Monod: it is time to increase the complexity of our predictive ecosystem models. Ecol. Model. 346, 77–87.

Klipp, E., Heinrich, R., Holzhutter, H.G., 2002. Prediction of temporal gene expression. Metabolic opimization by re-distribution of enzyme activities. Eur. J. Biochem. 269 (22), 5406–5413.

Klumpp, S., Zhang, Z., Hwa, T., 2009. Growth rate-dependent global effects on gene expression in bacteria. Cell 139, 1366–1375, http://dx.doi.org/10.1016/j.cell.2009.12.001.

Knoop, H., Gründel, M., Zilliges, Y., Lehmann, R., Hoffmann, S., Lockau, W., Steuer, R., 2013. Flux balance analysis of cyanobacterial metabolism: the metabolic network of Synechocystis sp. PCC 6803. PLoS Comput. Biol. 9 (6), e1003081, http://dx.doi.org/10.1371/journal.pcbi.1003081.

MacKenzie, T.D.B., Johnson, J.M., Cockshutt, A.M., Burns, R.A., Campbell, D.A., 2005. Large reallocations of carbon, nitrogen, and photosynthetic reductant among

phycobilisomes, photosystems, and Rubisco during light acclimation in *Synechococcus elongatus* strain PCC7942 are constrained in cells under low environmental inorganic carbon. Arch. Microbiol. 183, 190–202, http://dx.doi.org/10.1007/s00203-005-0761-1, ISSN 0302-8933.

Maitra, A., Dill, K.A., 2015. Bacterial growth laws reflect the evolutionary importance of energy efficiency. Proc. Natl. Acad. Sci. U. S. A. 112 (2), 406–411, http://dx.doi.org/10.1073/pnas.1421138111.

Mangan, N.M., Brenner, M.P., 2014. Systems analysis of the CO_2 concentrating mechanism in cyanobacteria. eLife 3, e02043, http://dx.doi.org/10.7554/eLife.02043.

Marcus, Y., Altman-Gueta, H., Finkler, A., Gurevitz, M., 2005. Mutagenesis at two distinct phosphate-binding sites unravels their differential roles in regulation of Rubisco activation and catalysis. J. Bacteriol. 187 (12), 222–4228, http://dx.doi.org/10.1128/jb.187.12. 4222-4228.2005.

Marr, A.G., 1991. Growth rate of *Escherichia coli*. Microbiol. Rev. 55 (2), 316–333.

McGinn, P.J., Price, G.D., Badger, M.R., 2004. High light enhances the expression of low-CO_2-inducible transcripts involved in the CO_2-concentrating mechanism in *Synechocystis* sp. PCC6803. Plant Cell Environ. 27 (5), 615–626, http://dx.doi.org/10.1111/j.1365-3040.2004.01175.x.

Megard, R.O., Tonkyn, D.W., Senft, W.H., 1984. Kinetics of oxygenic photosynthesis in planktonic algae. J. Plankton Res. 6 (2), 325–337, http://dx.doi.org/10.1093/plankt/6.2.325.

Molenaar, D., van Berlo, R., de Ridder, D., Teusink, B., 2009. Shifts in growth strategies reflect tradeoffs in cellular economics. Mol. Syst. Biol. 5, 323, http://dx.doi.org/10.1038/msb.2009.82.

Monod, J., 1949. The growth of bacterial cultures. Annu. Rev. Microbiol. 3, 371–394, http://dx.doi.org/10.1016/b978-0-12-460482-7.50020-8.

Mueller, T.J., Ungerer, J.L., Pakrasi, H.B., Maranas, C.D., 2017. Identifying the metabolic differences of a fast-growth phenotype in *Synechococcus* UTEX 2973. Sci. Rep. 7, 41569, http://dx.doi.org/10.1038/srep41569, ISSN 2045-2322.

Müller, S., Regensburger, G., Steuer, R., 2015. Resource allocation in metabolic networks: kinetic optimization and approximations by FBA. Biochem. Soc. Trans. 43 (6), 1195–1200.

Nedbal, L., Trtílek, M., Cervený, J., Komárek, O., Pakrasi, H.B., 2008. A photobioreactor system for precision cultivation of photoautotrophic microorganisms and for high-content analysis of suspension dynamics. Biotechnol. Bioeng. 100, 902–910, http://dx.doi.org/10.1002/bit.21833, ISSN 1097-0290.

Neidhardt, F.C., 1999. Bacterial growth: constant obsession with dn/dt. J. Bacteriol. 181, 7405–7408, ISSN 0021-9193.

Omata, T., Takahashi, Y., Yamaguchi, O., Nishimura, T., 2002. Structure, function and regulation of the cyanobacterial high-affinity bicarbonate transporter, BCT1. Funct. Plant Biol. 29 (3), 151–159.

Oren, A., 2014. Cyanobacteria An Economic Perspective – Cyanobacteria: Biology, Ecology and Evolution. John Wiley & Sons, pp. 12–13, Chapter 1.

Rügen, M., Bockmayr, A., Steuer, R., 2015. Elucidating temporal resource allocation and diurnal dynamics in phototrophic metabolism using conditional FBA. Sci. Rep. 5, 15247, http://dx.doi.org/10.1038/srep15247.

Raven, J.A., 2013. RNA function and phosphorus use by photosynthetic organisms. Front. Plant Sci. 4, 536, http://dx.doi.org/10.3389/fpls.2013.00536, ISSN 1664-462X.

Reimers, A.-M., Knoop, H., Bockmayr, A., Steuer, R., 2017. Cellular trade-offs and optimal resource allocation during cyanobacterial diurnal growth. Proc. Natl. Acad. Sci. U. S. A. 114 (31), E6457–E6465, http://dx.doi.org/10.1073/pnas.1617508114.

Saito, M.A., Goepfert, T.J., Ritt, J.T., 2008. Some thoughts on the concept of colimitation: three definitions and the importance of bioavailability. Limnol. Oceanogr. 53 (1), 276–290, http://dx.doi.org/10.4319/lo.2008.53.1.0276.

Schaechter, M., 2015. A brief history of bacterial growth physiology. Front. Microbiol. 6, 289, http://dx.doi.org/10.3389/fmicb.2015.00289, ISSN 1664-302X.

Scott, M., Gunderson, C.W., Mateescu, E.M., Zhang, Z., Hwa, T., 2010. Interdependence of cell growth and gene expression: origins and consequences. Science 330, 1099–1102, http://dx.doi.org/10.1126/science.1192588.

Tyystjärvi, E., 2008. Photoinhibition of photosystem II and photodamage of the oxygen evolving manganese cluster. Coord. Chem. Rev. 252 (3-4), 361–376, http://dx.doi.org/10.1016/j.ccr.2007.08.021.

Weiße, A.Y., Oyarzún, D.A., Danos, V., Swain, P.S., 2015. Mechanistic links between cellular trade-offs, gene expression, and growth. Proc. Natl. Acad. Sci. U. S. A. 112 (9), E1038–47, http://dx.doi.org/10.1101/014787.

Westermark, S., Steuer, R., 2016. Toward multiscale models of cyanobacterial growth: a modular approach. Front. Bioeng. Biotechnol. 4, 95, http://dx.doi.org/10.3389/fbioe.2016.00095.

Wijffels, R.H., Kruse, O., Hellingwerf, K.J., 2013. Potential of industrial biotechnology with cyanobacteria and eukaryotic microalgae. Curr. Opin. Biotechnol. 24 (June (3)), 405–413.

Worden, A.Z., Binder, B.J., 2003. Growth regulation of rRNA content in *Prochlorococcus* and *Synechococcus* (marine cyanobacteria) measured by whole-cell hybridization of rRNA-targeted peptide nucleic acids. J. Phycol. 39 (3), 527–534, http://dx.doi.org/10.1046/j.1529-8817.2003.01248.x.

Yu, J., Liberton, M., Cliften, P.F., Head, R.D., Jacobs, J.M., Smith, R.D., Koppenaal, D.W., Brand, J.J., Pakrasi, H.B., 2015. *Synechococcus elongatus* UTEX 2973: a fast growing cyanobacterial chassis for biosynthesis using light and CO_2. Sci. Rep. 5, 8132, http://dx.doi.org/10.1038/srep08132, ISSN 2045-2322.

Zavřel, T., Sinetova, M.A., Búzová, D., Literáková, P., Červený, J., 2015a. Characterization of a model cyanobacterium *Synechocystis* sp. PCC 6803 autotrophic growth in a flat-panel photobioreactor. Eng. Life Sci. 15 (1), 122–132, http://dx.doi.org/10.1002/elsc.201300165.

Zavřel, T., Sinetova, M.A., Červený, J., 2015b. Measurement of chlorophyll a and carotenoids concentration in cyanobacteria. J. Biotechnol. 5, 1–5 http://www.bio-protocol.org/e1467.

Zavřel, T., Červený, J., Knoop, H., Steuer, R., 2016. Optimizing cyanobacterial product synthesis: meeting the challenges. Bioengineered 7, 490–496, http://dx.doi.org/10.1080/21655979.2016.1207017, ISSN 2165-5987.

Zonneveld, C., 1997. Modeling effects of photoadaption on the photosynthesis-irradiance curve. J. Theor. Biol. 186 (3), 381–388, http://dx.doi.org/10.1006/jtbi.1997.0400.

SUPPLEMENTARY TEXT

A model of optimal protein allocation during phototrophic growth

Marjan Faizi, Tomáš Zavřel, Cristina Loureiro, Jan Červený, and Ralf Steuer

Contents

List of Figures

List of Tables

1 Model overview

We consider a coarse-grained model of proteome allocation in cyanobacteria to describe phototrophic growth. The model is described by ordinary differential equations (ODEs) and consists of the following processes and variables: uptake of external inorganic carbon (c_i^x) by a transporter protein T, conversion of the intracellular inorganic carbon pool (c_i) to amino acids (aa) by a metabolic multienzyme complex M, protein translation catalyzed by ribosomes R, and photosynthesis to produce energy units (e) that fuel all cellular processes. Energy production is implemented by activation of the photosystem unit (P^*) out of the inactivated state (P^0) due to light exposure. Energy production is restricted by product inhibition. In the extended version of the model external inorganic carbon c_i^x is also exchanged by passive diffusion and the activated photosynthetic unit P^* is subject to photodamage and degraded to amino acids. A schematic representation of the model is provided in figure 1 of the main text.

1.1 ODE System

The model is composed of 7 ODEs and one equation describing the growth rate. The ODEs are defined as follows

$$\frac{d[c_i]}{dt} = v_t - m_c \cdot v_m - \mu \cdot [c_i] \,,$$

$$\frac{d[aa]}{dt} = v_m - \mu \cdot [aa] - \sum_j n_j \gamma_j \,,$$

$$\frac{d[j]}{dt} = \gamma_j - \mu \cdot [j] \,,$$

$$\frac{d[e]}{dt} = m_\phi \cdot v_2 - v_t - m_\mu \cdot v_m - \mu \cdot [e] - m_\gamma \cdot \sum_j n_j \gamma_j \,,$$

and $\mu = \frac{1}{\mathcal{D}_c} \frac{v_t}{m_c}$.

$$v_t = [T] \cdot k_{cat}^t \cdot \frac{[c_i^x]}{K_t + [c_i^x]} \cdot \frac{[e]}{K_e + [e]}$$

$$v_m = [M] \cdot k_{cat}^m \cdot \frac{[c_i]}{K_m + [c_i]} \cdot \frac{[e]}{K_e + [e]}$$

$$\gamma_j = \beta_j \cdot \frac{\gamma_{\max}}{n_j} \cdot [R] \cdot \frac{[e]}{K_e + [e]} \cdot \frac{[aa]}{K_a + [aa]}$$

$$v_2 = \frac{k_2(e) \cdot \hat{\sigma} \cdot I \cdot [P]}{\hat{\sigma} \cdot I + k_2(e) + \mu}, \quad \text{with } k_2(e) = \frac{\tau}{1 + (\frac{[e]}{K_i})^4}$$

for $j \in \{R, T, M, P\}$

For the extended version of the model, including photodamage and diffusion, the following equations are modified

$$\frac{d[c_i]}{dt} = v_d + v_t - m_c \cdot v_m - \mu \cdot [c_i] \,,$$

$$\frac{d[aa]}{dt} = v_m + n_P \cdot v_i - \mu \cdot [aa] - \sum_j n_j \gamma_j \,,$$

$$\frac{d[P]}{dt} = \gamma_P - v_i - \mu \cdot [P] \,,$$

and $\mu = \frac{1}{\mathcal{D}_c} \frac{v_t + v_d}{m_c}$.

$$v_d = P_m \cdot A_{cell} \cdot (N \cdot [c_i^x] - \frac{[c_i]}{V_{cell}})$$

$$v_i = \frac{k_d \cdot \hat{\sigma}^2 \cdot I^2 \cdot [P]}{\hat{\sigma} \cdot I + k_2(e) + k_d \cdot \hat{\sigma} \cdot I + \mu}$$

$$v_2 = \frac{k_2(e) \cdot \hat{\sigma} \cdot I \cdot [P]}{\hat{\sigma} \cdot I + k_2(e) + k_d \cdot \hat{\sigma} \cdot I + \mu}$$

All intracellular concentrations are indicated by units of molecules per cell. All parameters are listed in table 1 in the main text, and further descriptions are given in section 3. A more detailed description for the ODEs and the definition of the growth rate is provided in section 2.

1.2 Model assumptions

In order to keep the model as simple as possible, we make the following assumptions: (i) we neglect protein degradation, and at least for higher growth rates it is reasonable to assume that the dilution term is significantly higher than protein degradation; (ii) the energy unit e is a surrogate for all energy containing compounds (here ATP, GTP and NADPH), whereby we assume an interconversion ratio of 2.6 ATP $\hat{=}$ 1 NADPH; (iii) we do not distinguish between CO_2 and HCO_3^- (or other forms of inorganic carbon); (iv) enzyme activity of RuBisCO is assumed to be the rate-limiting step during carbon metabolism; (v) half of the total cell mass is composed of proteins and only (approximately) half of the proteome is growth rate dependent; (vi) the cell volume and membrane surface are constant; (vii) photodamage affects the complete photosynthetic unit (as opposed to a repair cycle involving the D1 protein only).

2

2 Model description

2.1 Carbon metabolism

Carbon metabolism is represented by two steps: external inorganic carbon c_i^x is imported (v_t) into the cell by transporters T. Intracellular inorganic carbon c_i is then assimilated (v_m) into basic organic building blocks, here amino acids aa, that serve as precursor for protein synthesis. The synthesis of amino acids aa is catalyzed by a metabolic multienzyme complex M, which is composed of all enzymes that are required to catalyze the conversion from c_i to aa. We neglect an explicit CO_2 concentrating mechanism (CCM). We also do not distinguish between CO_2 or HCO_3^- and combine both as inorganic carbon c_i with the following dynamics

$$\frac{d[c_i]}{dt} = v_t - m_c \cdot v_m - \mu \cdot [c_i] \; , \tag{1}$$

with m_c denoting the number of c_i required to produce one amino acid. Both rates are described by Michaelis-Menten kinetics and depend on energy e

$$v_t = k_{\text{cat}}^t \cdot [T] \cdot \frac{[c_i^x]}{K_t + [c_i^x]} \cdot \frac{[e]}{K_e + [e]} \tag{2}$$

and

$$v_m = k_{\text{cat}}^m \cdot [M] \cdot \frac{[c_i]}{K_m + [c_i]} \cdot \frac{[e]}{K_e + [e]} \; , \tag{3}$$

where k_{cat}^t and k_{cat}^m are the maximal turnover rates of the transporter and metabolic enzyme, and K_t and K_m the corresponding half-saturation constants of both enzymes. The half-saturation constant K_e is, for simplicity, the same for all energy dependent reactions.

For the extended version of the model, we also considered nutrient uptake via diffusion. The amount of c_i^x that diffuses (v_d) through the cell depends on the permeability of the cell membrane P_m, the cell surface A_{cell} and the gradient of internal and external c_i

$$v_d = P_m \cdot A_{cell} \cdot (N_A \cdot [c_i^x] - \frac{[c_i]}{V_{cell}}) \; , \tag{4}$$

whereby V_{cell} and N_A are the cell volume and Avogadro constant, respectively, and are required to convert the units of c_i and c_i^x into numbers of molecules per liter, additionally A_{cell} and V_{cell} are, for simplicity, assumed to be constant. Hence, for the extended model the diffusion term v_d must be added to equation (1)

$$\frac{d[c_i]}{dt} = v_t + v_d - m_c \cdot v_m - \mu \cdot [c_i] \; . \tag{5}$$

2.2 Protein translation

Protein translation is modeled according to [1, 2]. Proteins are translated by ribosomes R, whereby amino acids aa serve as a precursor for protein synthesis and are produced (v_m) themselves out of inorganic carbon

$$\frac{d[aa]}{dt} = v_m - \mu \cdot [aa] - \sum_{j \in \{R,T,M,P\}} n_j \cdot \gamma_j \; , \tag{6}$$

where γ_j denotes the translation rate of protein complex j and n_j the size of the respective protein complex (in units of amino acids). In addition, translation depends here not only on availability of amino acids but also consumes energy. The translation rate γ_j for each protein complex j is described by

$$\gamma_j = \beta_j \cdot \frac{\gamma_{\max}}{n_j} \cdot [R] \cdot \frac{[e]}{K_e + [e]} \cdot \frac{[aa]}{K_a + [aa]} \; , \tag{7}$$

where $\gamma_{\max}$, denoting the maximal elongation rate, is divided by the size of the protein complex, since larger complexes take longer to translate. K_a indicates the half-saturation constant of ribosomes for amino acids and the factor β_j denotes the fraction of total ribosomes that are allocated to the translation of protein complex j and fulfills the constraint

$$\sum_{j \in \{R,T,M,P\}} \beta_j \leq 1 \; , \; \forall j : \beta_j \geq 0 \; . \tag{8}$$

The dynamics for the protein complexes R, T, and M are described by the equations

$$\frac{d[R]}{dt} = \gamma_R - \mu \cdot [R] \ , \tag{9}$$

$$\frac{d[T]}{dt} = \gamma_T - \mu \cdot [T] \ , \tag{10}$$

and

$$\frac{d[M]}{dt} = \gamma_M - \mu \cdot [M] \ . \tag{11}$$

2.3 Photosynthesis

The conversion of light into cellular energy is described by a minimal model of a photosynthetic unit, following the model of Han [3]. A photosynthetic unit is defined as an assembly of light-harvesting complexes (photosystem-I and -II) and an electron transport chain involved in the evolution of molecular oxygen [3]. The photosynthetic unit P exists in two states: inactivated P^0 and activated P^*. Light I facilitates the transition (v_1) to the activated state P^*, which then is involved in producing (v_2) energy e. The respective equations are

$$\frac{d[P^0]}{dt} = \gamma_P - v_1 + v_2 - \mu \cdot [P^0] \tag{12}$$

and

$$\frac{d[P^*]}{dt} = v_1 - v_2 - \mu \cdot [P^*] \ . \tag{13}$$

The fast transitions between both states of the photosynthetic unit are described by mass-action kinetics

$$v_1 = \hat{\sigma} \cdot I \cdot [P^0] \tag{14}$$

and

$$v_2 = k_2(e) \cdot [P^*] \ , \tag{15}$$

with

$$k_2(e) = \frac{\tau}{1 + (\frac{[e]}{Ki})^4} \tag{16}$$

where τ denotes the maximum turnover rate of the photosynthetic unit and $\hat{\sigma}$ the effective absorption cross-section, which determines the surface that is capable of absorbing a certain amount of photons. Additionally, v_2 contains a self-inhibition term for e, with an inhibition constant K_i, to regulate its own production, since energy production is not restricted by any other mechanism. Furthermore, we consider the dynamics of the concentration of the total photosynthetic unit to be $[P] = [P^0] + [P^*]$, so that

$$\frac{d[P]}{dt} = \gamma_P - \mu \underbrace{\left([P^0] + [P^*]\right)}_{[P]} \tag{17}$$

and assume a quasi-steady state for its activated form

$$\frac{d[P^*]}{dt} = 0 \iff [P^*] = \frac{\hat{\sigma} \cdot I \cdot [P]}{\hat{\sigma} \cdot I + k_2(e) + \mu} \ . \tag{18}$$

The rate of energy production is then $m_\phi \cdot v_2$, with m_ϕ determining the number of molecules produced per cycle, and

$$v_2 = k_2(e) \cdot [P^*] = \frac{k_2(e) \cdot \hat{\sigma} \cdot I \cdot [P]}{\hat{\sigma} \cdot I + k_2(e) + \mu} \ . \tag{19}$$

Thus, the energy balance with respect to e is given by the equation

$$\frac{d[e]}{dt} = m_\phi \cdot v_2 - v_{\mathrm{t}} - m_\mu \cdot v_{\mathrm{m}} - \mu \cdot [e] - m_\gamma \cdot \sum_{j \in \{R,T,M,P\}} n_j \cdot \gamma_j \ , \tag{20}$$

where m_μ and m_γ denote the number of e molecules required to produce one amino acid or for one translation elongation step, respectively. We note that the cellular component e combines

contributions from ATP, GTP and NADPH, and is assumed to have no carbon backbone but is only "recharged".

The coarse-grained model is extended with the capability to exhibit photoinhibition, which is a decline in the photosynthetic capacity and a result of high light intensities that damage the photosystem-II [4]. Applying this process to our model means that the photosynthetic unit can be damaged within the active state P^* and subsequently degraded to amino acids. The photoinhibition rate (v_i) is then calculated as follows (and happens at all light intensities proportional to the light intensity)

$$v_i = k_d \cdot \hat{\sigma} \cdot I \cdot [P^*] \;, \tag{21}$$

where k_d is the photodamge rate of the photosynthetic unit. Adding equation (21) to the definition of equation (18) yields

$$[P^*] = \frac{\hat{\sigma} \cdot I \cdot [P]}{\hat{\sigma} \cdot I + k_2(e) + k_d \cdot \hat{\sigma} \cdot I + \mu} \;, \tag{22}$$

and equation (17) is then modified to

$$\frac{d[P]}{dt} = \gamma_P - v_i - \mu \cdot [P] \;, \tag{23}$$

with

$$v_i = \frac{k_d \cdot \hat{\sigma}^2 \cdot I^2 \cdot [P]}{\hat{\sigma} \cdot I + k_2(e) + k_d \cdot \hat{\sigma} \cdot I + \mu} \;. \tag{24}$$

Furthermore, equation (6) gets an additional term, as the photosynthetic unit degrades back to amino acids

$$\frac{d[aa]}{dt} = v_m + n_P \cdot v_i - \mu \cdot [aa] - \sum_{j \in \{R,T,M,P\}} n_j \cdot \gamma_j \;. \tag{25}$$

2.4 Modeling bacterial growth

To study how the cell adapts its macromolecule composition on the basis of changing external conditions (I and c_i^x), we applied the ODE model to a nonlinear optimization problem. The optimization task is to find the proteome distribution, by adjusting the proportion of ribosomes β_j that are allocated to translate protein type j, that maximizes the (steady-state) growth rate (balanced growth). To simulate the ODE model, we use the parameters described below in section 3 (and are listed in table 1 of the main text). To ensure that the cell is forced to reallocate its proteome distribution for changing external conditions, the protein mass per cell volume is restricted to a fixed value and assumed to be approximately constant across different growth rates [5, 6]. Furthermore, we assume that the cell mass is proportional to the proteome mass, and therefore, define the total cell density $\mathcal{D}_c$ as weighted sum of all components in numbers of amino acids per cell (except for e which adds no weight to the mass)

$$\mathcal{D}_c = \frac{[c_i]}{m_c} + [aa] + \sum_{j \in \{R,T,M,P\}} n_j \cdot [j] \;, \tag{26}$$

thus, by applying the steady-state assumption, we obtain

$$\frac{d\mathcal{D}_c}{dt} = 0 \iff \frac{1}{m_c} \cdot \frac{d[c_i]}{dt} + \frac{d[aa]}{dt} + \sum_{j \in \{R,T,M,P\}} n_j \cdot \frac{d[j]}{dt} = 0 \;, \tag{27}$$

and after conversion

$$\mu \cdot \underbrace{(\frac{[c_i]}{m_c} + [aa] + \sum_{j \in \{R,T,M,P\}} n_j \cdot [j])}_{\mathcal{D}_c} = \frac{v_t}{m_c} \;. \tag{28}$$

Hence, the growth rate is defined as

$$\mu = \frac{v_t}{m_c \cdot \mathcal{D}_c} \;, \tag{29}$$

which serves as objective function for the optimization problem with respect to equation (8). Recalculating the growth rate for the extended model, including photoinhibition and diffusion, modifies equation (29) as follows

$$\mu = \frac{v_t + v_d}{m_c \cdot \mathcal{D}_c} \;. \tag{30}$$

3 Model Parameters

3.1 Stoichiometric coefficients

Carbon metabolism. The active transport of one external inorganic carbon via the bicarbonate transporter requires one ATP molecule. The production of one amino acid, with an average carbon chain length of $m_c = 5$, requires 17.9 ATP and 10.31 NADPH molecules, hence in total approximately $m_\mu = 45$ energy units (calculated using the metabolic network of Knoop et al. [7]).

Protein translation. We assume that each translational elongation step requires one ATP and two GTP molecules, which results in total in $m_\gamma = 3$ energy units (and one aa).

Photosynthesis. We further assume, based on the stoichiometric reconstruction [7], that each electron transport flow of the photosynthetic unit generates 2.6 ATP and 2 NAPDH molecules (normalized to the formation of one oxygen molecule), which equals to approximately $m_\phi = 8$ energy units.

3.2 Protein lengths

To determine the lengths for the four protein classes, we selected the model organism *Synechocystis sp.* PCC 6803 (hereafter called *Synechocystis*). The protein lengths of the ribosome, transporter and photosynthetic unit are determined using the UniProt database [8].

3.2.1 Ribosome R

All ribosomal protein subunits and their stoichiometry are listed in table T2 and T3. Each subunit appears once per ribosome, except for protein L7/L12, for which 4 copies are determined in *E.coli* [9], and both homologue proteins of S1 are counted as half. We do not take ribosomal RNA into account, since we only consider proteins for our cell mass. In total this sums up to a ribosome length of about 7358 amino acids.

3.2.2 Transporter T

The ATP-dependent bicarbonate transporter in *Synechocystis* represents our transporter enzyme (T) that facilitates c_i^x uptake and has a length of 1681 amino acids (see table T4).

3.2.3 Metabolic multienzyme complex M

We calculated the average amino acid length of a metabolic enzyme to be 345.77 with the genome-scale metabolic network of *Synechocystis* from Knoop et al. [7]. In addition, we calculated with this model the number of steps to convert inorganic carbon into an average amino acid, namely 82.8 steps. Thus, our metabolic multienzyme complex amounts to approximately 28630 amino acids.

3.2.4 Photosynthetic unit P

The photosynthetic unit is composed of all important proteins necessary for the photosynthetic electron flow [10], namely photosystem-I (PS–I) and -II (PS–II) including the light-harvesting complex phycobilisome, cytochrome b_6f, plastocyanin, ferredoxin-NADP$^+$ reductase (FNR) and ATP-synthase. According to the number of times the proteins are used to facilitate the transport of the electrons produced per formation of one oxygen molecule, the ratios within one photosynthetic unit are determined as follows: (i) 4· PS–I; (ii) 1· PS–II + phycobilisome; (iii) 2· cytochrome b$_6$f; (iv) 4· plastocyanin; (v) 4· FNR and (vi) $\frac{12}{14}$· ATP–synthase.
To determine the subunit stoichiometry of the phycobilisome, we follow the structural description of [11]. The PS–I complex exists in cyanobacteria in monomeric, dimeric and trimeric form [12], therefore we choose on average a dimeric form for PS–I. Additionally, the PS–II complex is accounted as a dimer. By considering the compositions of all proteins and their stoichiometry, listed in table T5-T9, this sums up to a protein length of approximately 95451 amino acids per photosynthetic unit.

3.3 Parameter estimation

Cell density. We assume that the cell density $\mathcal{D}_c$ is proportional to the proteome mass per cell volume. To calculate the proteome mass, we further assume that approximately half of the cell mass consists of proteins (following the biomass objective function used in Knoop et al. [7]). From the experimental measurements in table T1, we calculate the dry weight per cell and convert half of it into units of amino acids per cell. Additionally, we assume that there is a non-growth related proteome fraction of approximately 50% that does not contribute to growth [13]. Hence, the cell density $\mathcal{D}_c$ (in units of amino acids per cell volume), which is assumed to be proportional to the growth-related proteome mass per cell, is defined as follows

$$\mathcal{D}_c = 0.25 \cdot \frac{10^{-3} \cdot dry\ weight\ \left[\frac{mg}{L\ (culture)}\right]}{cell\ count\ \left[\frac{cells}{L\ (culture)}\right]} \cdot \frac{N}{100\left[\frac{Da}{aa}\right]} \quad , \tag{31}$$

where *dry weight* and *cell count* are the mean values taken from table T1. The results for each light intensity are plotted in figure S1. We therefore assume a value of $\mathcal{D}_c = 1.4 \cdot 10^{10}$ amino acids per cell.

Energy and amino acid threshold. The one-half-saturation constants for energy molecules during transport, metabolism and translation (K_e) and for amino acids (K_a) are chosen equal for simplicity and selected in such a way that they prevent energy and amino acid from becoming negative during the numerical computations.

Diffusion. The cell surface and volume (A_{cell} and V_{cell}) are required to convert the components of the diffusion term, hence to calculate them, we assume an average cell radius of 1.75 μm. To calculate the cell radius, we assume a constant dry weight per cell of 8.67 pg (average of all dry weight values in table T1). Assuming further that the dry mass per volume is $0.3 - 0.5$ pg/μm^3 [14], leads to a cell volume of $17.35 - 28.91$ μm^3 and consequently also to a cell radius of $1.6 - 1.9$ μm. Furthermore, we assume that the permeability of c_i^x corresponds to the permeability of bicarbonate molecules HCO_3^- [15], since most of the inorganic carbon at least in seawater is in the form of HCO_3^- and dissolved CO_2 represents only a small fraction of less than 1% [16].

Photosynthesis. To determine the remaining parameters of the photosynthetic part of the model (τ, $\hat{\sigma}$ and k_d), we set the external inorganic carbon concentration to a fixed value $[c_i^x] = 1000$ μM (2000 μM is observed in seawater [17]), however, we assume a lower concentration in the medium because of the higher density of cells compared to seawater conditions). We estimate the parameters by fitting the model to the experimental data given in table T1. In order to get a better sense of what order of magnitude the parameters are, we followed the model of Han [18], where the photodamage kd ranges between $0 - 10^{-7}$, the effective absorption cross-section $\hat{\sigma}$ between $0.6 - 3.0$ $m^2/\mu E$ and the turnover rate of the photosynthetic unit τ between $1000 - 10000$ s^{-1}. However, those parameter ranges are too high for our model, meaning that the resulting growth curve is far above the experimental measurements. Therefore, we chose different boundaries for our parameters and figure S2 shows the range of possible growth curves that can be simulated with the following ranges

$$\hat{\sigma} = 0.1 - 0.3\ \left[\frac{m^2}{\mu E}\right], \quad k_d = 10^{-6} - 5 \cdot 10^{-6} \quad \text{and} \quad \tau = 1000 - 4000\ [min^{-1}].$$

In this region we searched for those parameters $\hat{\sigma}$, k_d and τ that minimize the distance between experimental and simulated growth rates. Therefore we minimize the negative logarithm of the likelihood $l(\theta)$ as follows

$$l(\theta) = \sum_i [(\frac{y_i(\theta) - x_i}{\sigma_i})^2 + log(2\pi\sigma_i^2)] \quad , \tag{32}$$

where x_i represents the experimental data with their uncertainties σ_i and $y(\theta)_i$ denotes the simulated data points calculated with the model parameters θ. Figure S2 shows the best fit with $l(\theta) = -61.43$, obtained with the parameters: $\tau = 1900\ [min^{-1}]$, $\hat{\sigma} = 0.166\ \left[\frac{m^2}{\mu E}\right]$ and $k_d = 1.6 \cdot 10^{-6}$.

Subsequently, we compared the oxygen evolution rate with the energy production rate v_2, to test the model performance. The oxygen evolution rate v_{O_2} is defined as the difference between photosynthesis v_{photo} and respiration rate v_{resp} (see table T1). The energy production rate v_2 is

described in units of molecules per cell per time, while the oxygen evolution rate v_{O_2} is normalized to the amount of dry weight

$$v_{O_2}[\mu mol(O_2)\ mg^{-1}s^{-1}] = (v_{photo} - v_{resp}) \cdot \frac{10^{-3} \cdot chlorophyll\ a}{dry\ weight} \quad .$$
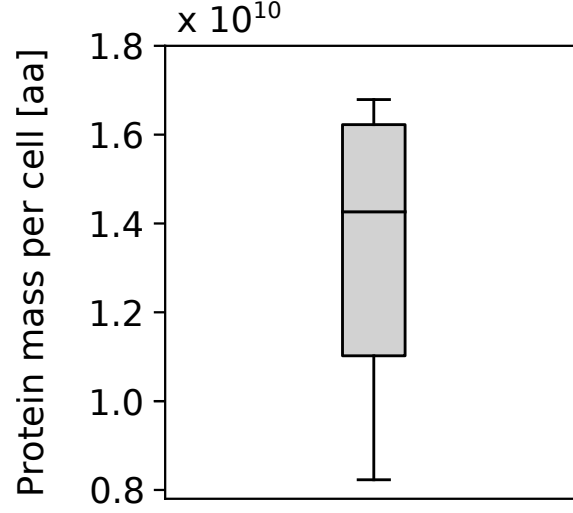
(33)

4 Supplementary Figures and Tables

Figure S1: Estimation of protein mass. We calculated the total protein mass as 50% of the dry weight per cell and converted it into units of amino acids (aa). Additionally, we assume that 50% of the proteome does not contribute to growth. The total protein mass is plotted for each light intensity from Table T1, whereby we only considered the mean values. The median is around $1.4 \cdot 10^{10}$ [aa per cell].
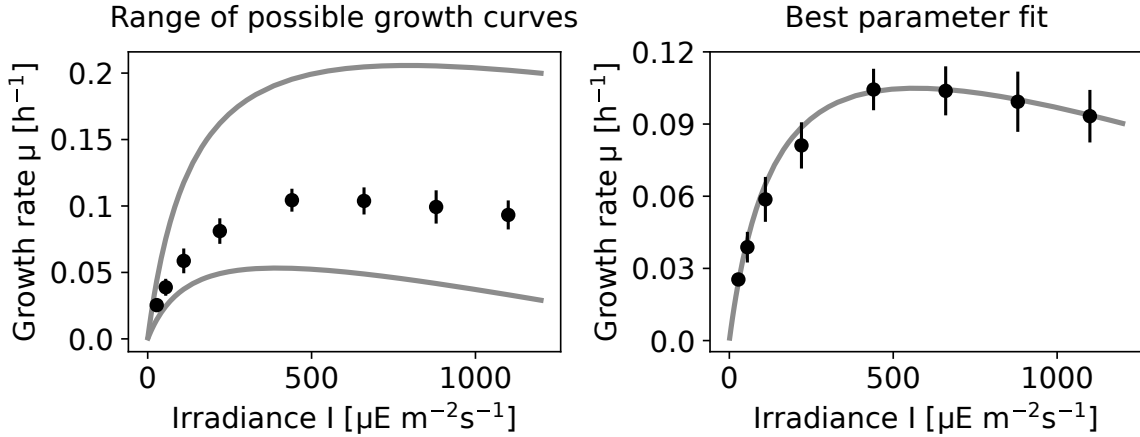
Figure S2: Parameter fitting of the photosynthetic part. Experimental data (black circle) in comparison to simulated growth curves (solid gray line) with different parameter sets for the turnover rate of the photosystem (τ), photodamage rate (k_d) and effective absorption cross-section ($\hat{\sigma}$). The left plot shows the range of growth curves that can be simulated within the parameter boundaries. The lower left curve is simulated with $\tau = 1000$, $k_d = 2.5 \cdot 10^{-6}$ and $\hat{\sigma} = 0.1$, while the upper growth curve is simulated with $\tau = 4000$, $k_d = 10^{-6}$ and $\hat{\sigma} = 0.3$. The best fit on the right plot is obtained with $\tau = 1900$, $k_d = 1.6 \cdot 10^{-6}$ and $\hat{\sigma} = 0.166$. All model simulations are performed with $c_i^x = 1000$ μM.
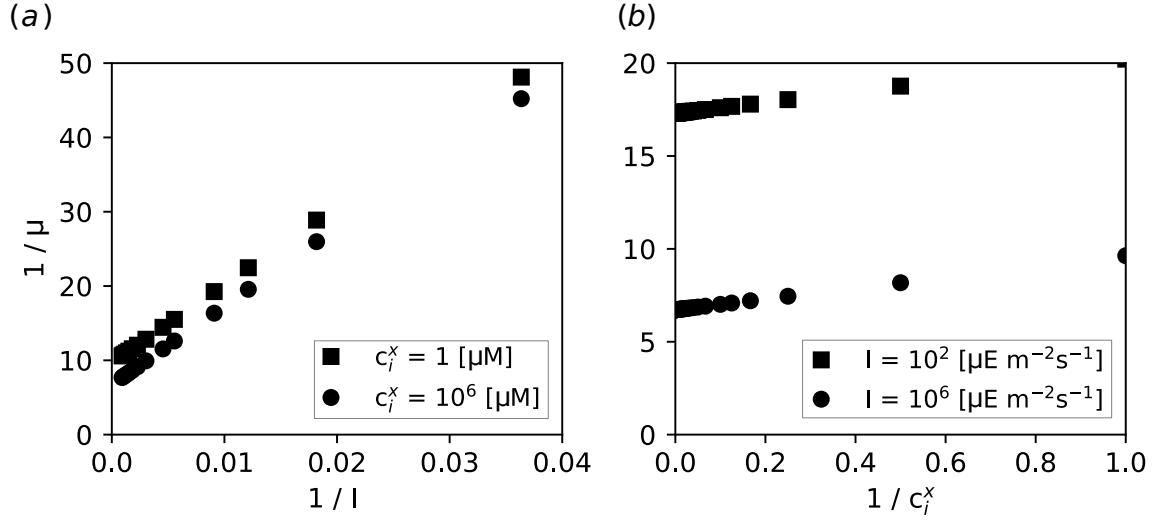
Figure S3: Lineweaver-Burk plot. A Lineweaver–Burk (LB) plot is a double reciprocal plot of growth rate versus light intensity and carbon availability. Parallel lines in the LB plot are characteristic for uncompetitive inhibition (limitation by external inorganic carbon or light acts as an uncompetitive inhibitor and lowers the apparent K_m and V_m values for the other nutrient). μ: growth rate [h^{-1}], I: Irradiance [μE m^{-2}s^{-1}] and c$_i^x$: external inorganic carbon [μM].
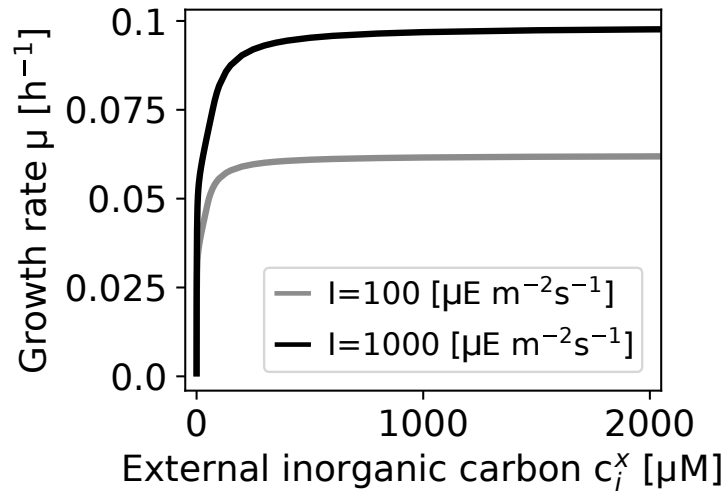
Figure S4: Growth as a function of c_i^x in the extended model. Growth rates are simulated for two different light intensities (I). Due to the diffusion term in the extended model the growth curve for increasing c_i^x does not follow a Monod-like shape.
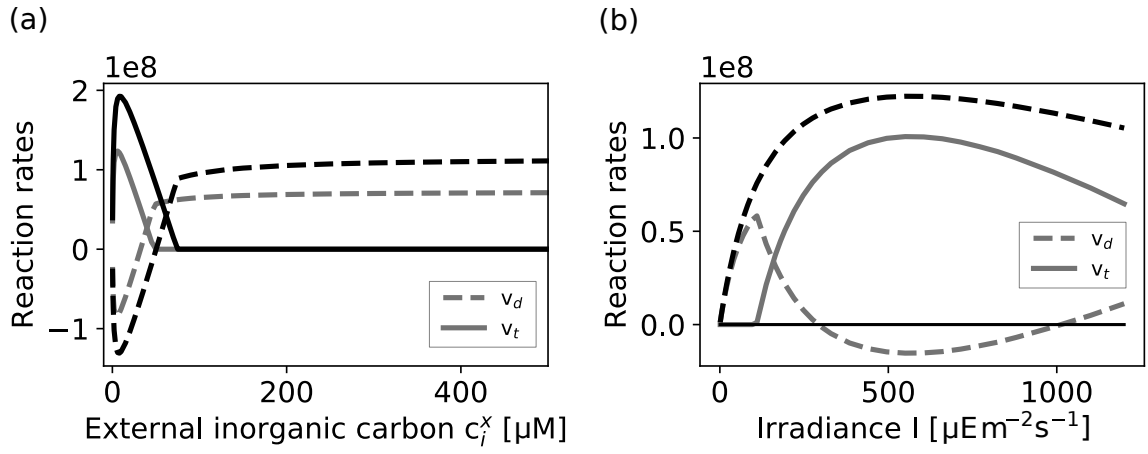
Figure S5:   Carbon uptake rates. Shown is active carbon transport rate (v_t, solid line) and the diffusion rate (v_d, dashed line) for different external conditions. **(a)** Reaction rates for increasing external inorganic carbon c_i^x and two (constant) light intensities, $I = 100 \ \mu$E m^{-2}s^{-1} (gray curve) and $I = 1000 \ \mu$E m^{-2}s^{-1} (black curve), respectively. For low external carbon, carbon uptake is facilitated by active transport, whereas passive diffusion results in a net loss of inorganic carbon (carbon cycling). As the concentration of external inorganic carbon increases, the required activity of the transport decreases. At some point, the direction of diffusion changes sign and results in a net import of inorganic carbon into the cell. For high external inorganic carbon, the transport is not expressed. **(b)** Reaction rates for increasing light intensity I and two (fixed) concentrations of c_i^x, $c_i^x = 50 \ \mu$M (gray curve) and $c_i^x = 1000 \ \mu$M (black curve), respectively. For low light (and hence slow growth), the demand for inorganic carbon is met by passive diffusion. For a critical light intensity, and low inorganic carbon (gray line), active transport is induced.
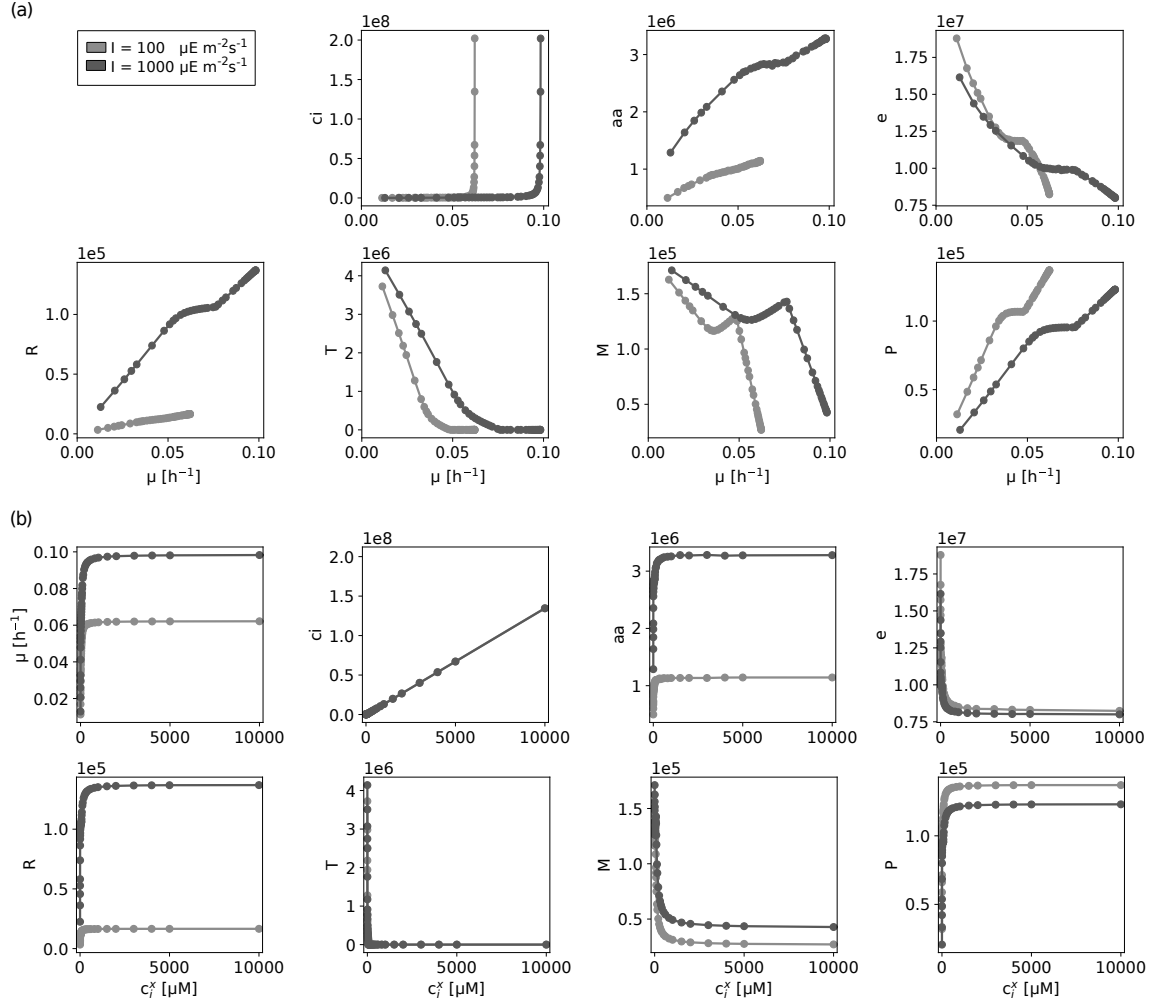
Figure S6: Concentrations of intracellular compounds for increasing c_i^x (extended model). Molecules per cell are displayed (a) as a function of growth rate μ, and (b) as a function of external inorganic carbon c_i^x for two different light conditions. ci: inorganic carbon; aa: amino acid; e: energy unit; R: ribosome; T: transporter; M: metabolic enzyme; P: photosynthetic unit.
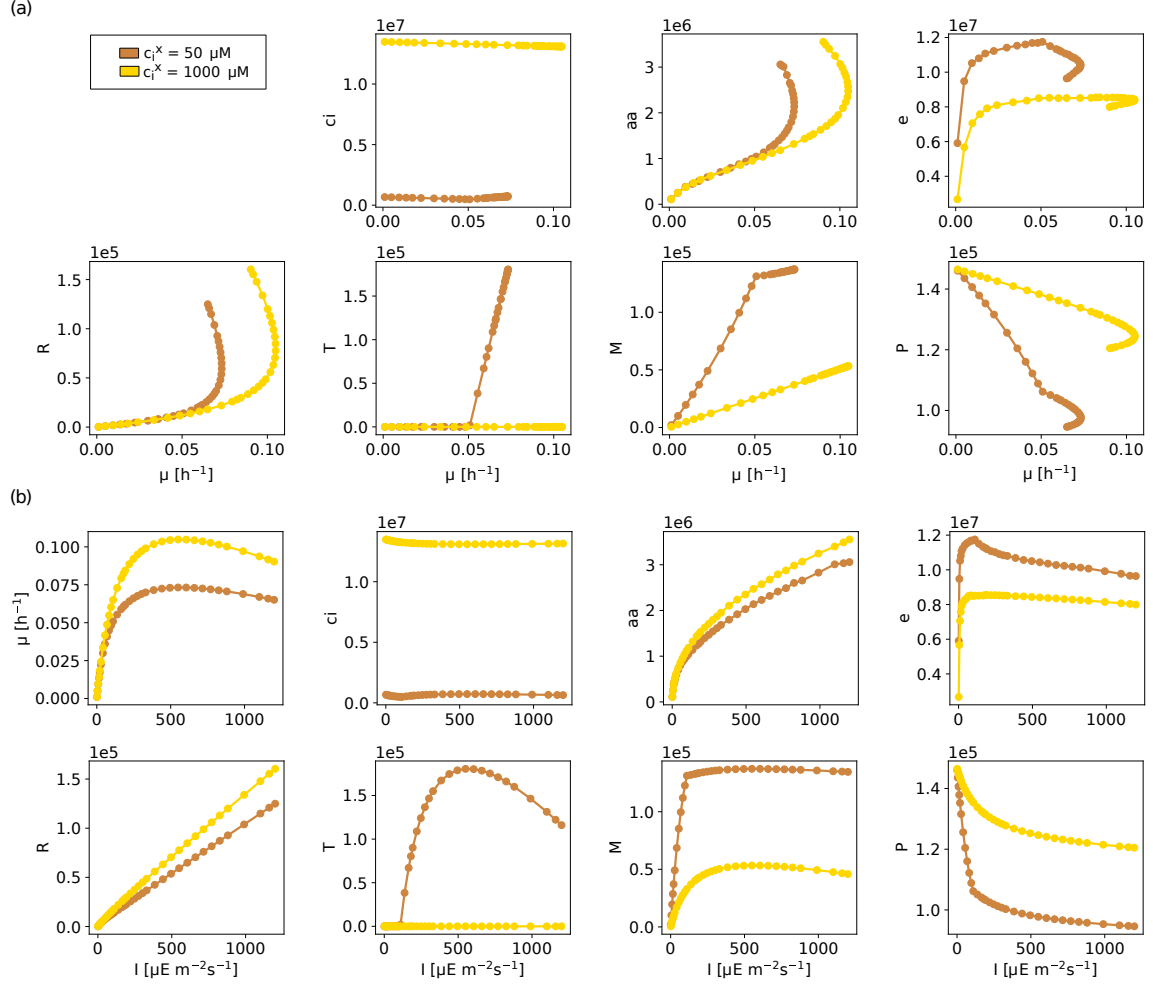
Figure S7: Concentrations of intracellular compounds for increasing I (extended model). Molecules per cell are displayed (a) as a function of growth rate μ (b), as a function of light intensity I for two different c_i^x concentrations in both panels. Notably, the mass-fraction of ribosomes increase linearly as a function of light intensity. ci: inorganic carbon; aa: amino acid; e: energy unit; R: ribosome; T: transporter; M: metabolic enzyme; P: photosynthetic unit.

13

Table T1: Data obtained for *Synechocystis* 6803 sub-strain (GT-L) using controlled turbidostat experiments.

red light [μE m^{-2}s^{-1}]		27.5	55	110	220
specific growth rate [h^{-1}]	mean	0.02540	0.03882	0.05869	0.08112
	sd	0.00178	0.00637	0.00933	0.00961
chlorophyll (a) [μmol L(culture)$^{-1}$]	mean	2.36657	2.53722	2.22747	2.26997
	sd	0.28530	0.22823	0.21533	0.22739
dry weight [mg L(culture)$^{-1}$]	mean	132.200	165.583	173.000	219.562
	sd	39.7816	58.4965	29.0517	50.1615
cell count [cells L(culture)$^{-1}$]	mean	2.52E10	2.54E10	2.14E10	2.10E10
	sd	2.98E09	3.31E09	4.94E09	2.11E09
photosynthesis [μmol(O$_2$) mmol(Chl)$^{-1}$s^{-1}]	mean	30.4787	42.5266	80.6806	119.475
	sd	5.65365	6.90414	11.7693	19.0497
respiration [μmol(O$_2$) mmol(Chl)$^{-1}$s^{-1}]	mean	-5.45712	-6.43310	-12.3565	-18.9473
	sd	2.70102	1.11482	5.97641	2.29437

| red light [μE m^{-2}s^{-1}]		440	660	880	1100
specific growth rate [h^{-1}]	mean	0.10436	0.10380	0.09928	0.09327
	sd	0.00862	0.01019	0.01252	0.01092
chlorophyll (a) [μmol L(culture)$^{-1}$]	mean	1.93189	1.88480	1.67495	1.49722
	sd	0.05443	0.18380	0.13364	0.15200
dry weight [mg L(culture)$^{-1}$]	mean	221.375	259.750	256.375	230.857
	sd	15.1183	19.2635	21.5460	58.6158
cell count [cells L(culture)$^{-1}$]	mean	2.56E10	2.30E10	2.43E10	2.68E10
	sd	2.02E09	4.45E09	4.30E09	4.46E09
photosynthesis [μmol(O$_2$) mmol(Chl)$^{-1}$s^{-1}]	mean	184.629		251.599	
	sd	24.7217		49.4417	
respiration [μmol(O$_2$) mmol(Chl)$^{-1}$s^{-1}]	mean	-24.6819		-40.9372	
	sd	7.61381		14.6008	

Table T2: Ribosomal proteins in *Synechocystis* 6803 (large subunits).

Uniprot ID	Gene name	Protein name	Stoichiometry	Length
P36236	rplA	50S ribosomal protein L1	1	238
P73317	rplB	50S ribosomal protein L2	1	276
P73320	rplC	50S ribosomal protein L3	1	213
P73319	rplD	50S ribosomal protein L4	1	210
P73308	rplE	50S ribosomal protein L5	1	180
P73306	rplF	50S ribosomal protein L6	1	179
P42352	rplI	50S ribosomal protein L9	1	152
P23350	rplJ	50S ribosomal protein L10	1	173
P36237	rplK	50S ribosomal protein L11	1	141
P23349	rplL	50S ribosomal protein L7/L12	4	128
P73294	rplM	50S ribosomal protein L13	1	151
P73310	rplN	50S ribosomal protein L14	1	122
P73303	rplO	50S ribosomal protein L15	1	147
P73313	rplP	50S ribosomal protein L16	1	139
P73296	rplQ	50S ribosomal protein L17	1	116
P73305	rplR	50S ribosomal protein L18	1	120
P36239	rplS	50S ribosomal protein L19	1	122
P48957	rplT	50S ribosomal protein L20	1	117
P74266	rplU	50S ribosomal protein L21	1	124
P73315	rplV	50S ribosomal protein L22	1	121
P73318	rplW	50S ribosomal protein L23	1	101
P73309	rplX	50S ribosomal protein L24	1	115
P73289	rplY	50S ribosomal protein L25	1	98
P74267	rpmA	50S ribosomal protein L27	1	87
P72851	rpmB	50S ribosomal protein L28	1	78
P73312	rpmC	50S ribosomal protein L29	1	73
P73292	rpmE	50S ribosomal protein L31	1	81
P73014	rpmF	50S ribosomal protein L32	1	57
P48958	rpmG	50S ribosomal protein L33	1	65
Q55004	rpmH	50S ribosomal protein L34	1	45
P48959	rpmI	50S ribosomal protein L35	1	67
P73300	rpmJ	50S ribosomal protein L36	1	38
Total				4458

Table T3: Ribosomal proteins in *Synechocystis* 6803 (small subunits).

Uniprot ID	Gene name	Protein name	Stoichiometry	Length
P73530	rps1A	30S ribosomal protein S1 homolog A	0.5	328
P74142	rps1b	30S ribosomal protein S1 homolog B	0.5	305
P74071	rpsB	30S ribosomal protein S2	1	269
P73314	rpsC	30S ribosomal protein S3	1	240
P48939	rpsD	30S ribosomal protein S4	1	202
P73304	rpsE	30S ribosomal protein S5	1	173
P73636	rpsF	30S ribosomal protein S6	1	113
P74229	rpsG	30S ribosomal protein S7	1	156
P73307	rpsH	30S ribosomal protein S8	1	133
P73293	rpsI	30S ribosomal protein S9	1	137
P74226	rpsJ	30S ribosomal protein S10	1	105
P73298	rpsK	30S ribosomal protein S11	1	130
P74230	rpsL	30S ribosomal protein S12	1	126
P73299	rpsM	30S ribosomal protein S13	1	127
P48944	rpsN	30S ribosomal protein S14	1	100
P72866	rpsO	30S ribosomal protein S15	1	89
P74410	rpsP	30S ribosomal protein S16	1	82
P73311	rpsQ	30S ribosomal protein S17	1	81
P48946	rpsR	30S ribosomal protein S18	1	71
P73316	rpsS	30S ribosomal protein S19	1	92
P73336	rpsT	30S ribosomal protein S20	1	97
P48949	rpsU	30S ribosomal protein S21	1	60
Total				2899.5

Table T4: Bicarbonate transporter in *Synechocystis* 6803.

Uniprot ID	Gene name	Protein name	Stoichiometry	Length
Q55460	cmpA	Bicarbonate-binding protein CmpA	1	452
Q55461	cmpB	Bicarbonate transport system permease protein CmpB	1	280
Q55462	cmpC	Bicarbonate transport ATP-binding protein CmpC	1	667
Q55463	cmpD	Bicarbonate transport ATP-binding protein CmpD	1	282
Total				1681

Table T5: Photosystem-I monomer in *Synechocystis* 6803.

Uniprot ID	Gene name	Protein name	Stoichiometry	Length
P29254	psaA	Photosystem I P700 chlorophyll a apoprotein A1 (PsaA)	1	751
P29255	psaB	Photosystem I P700 chlorophyll a apoprotein A2 (PsaB)	1	731
P32422	psaC	Photosystem I iron-sulfur center (Photosystem I subunit VII) (PsaC)	1	81
P19569	psaD	Photosystem I reaction center subunit II (PSI-D)	1	141
P12975	psaE	Photosystem I reaction center subunit IV (p30 protein)	1	74
P29256	psaF	Photosystem I reaction center subunit III (PSI-F)	1	165
Q55330	psaI	Photosystem I reaction center subunit VIII	1	40
Q55329	psaJ	Photosystem I reaction center subunit IX	1	40
P72712	psaK1	Photosystem I reaction center subunit PsaK 1 (Photosystem I subunit X 1)	1	86
P74564	psaK2	Photosystem I reaction center subunit PsaK 2 (Photosystem I subunit X 2)	1	90
P37277	psaL	Photosystem I reaction center subunit XI (PSI-L)	1	157
P72986	psaM	Photosystem I reaction center subunit XII (PSI-M)	1	31
Total				2387

Table T6: Photosystem-II monomer in *Synechocystis* 6803.

Uniprot ID	Gene name	Protein name	Stoichiometry	Length
P74367	psb27	Photosystem II lipoprotein Psb27	1	134
Q55356	psb28	Photosystem II reaction center Psb28 protein (Photosystem II reaction center W protein)	1	112
P07826	psbA1	Photosystem II protein D1 1 (PSII D1 protein 1) (Photosystem II Q(B) protein 1)	1	360
P16033	psbA2	Photosystem II protein D1 2 (PSII D1 protein 2) (Photosystem II Q(B) protein 2)	1	360
P05429	psbB	Photosystem II CP47 reaction center protein (Protein CP-47)	1	507
P09193	psbC	Photosystem II CP43 reaction center protein (Protein CP-43)	1	460
P09192	psbD	Photosystem II D2 protein (PSII D2 protein) (Photosystem Q(A) protein)	1	352
P09190	psbE	Cytochrome b559 subunit alpha (PSII reaction center subunit V)	1	81
P09191	psbF	Cytochrome b559 subunit beta (PSII reaction center subunit VI)	1	44
P14835	psbH	Photosystem II reaction center protein H (PSII-H)	1	64
Q54697	psbI	Photosystem II reaction center protein I (PSII-I)	1	38
P73070	psbJ	Photosystem II reaction center protein J (PSII-J)	1	39
P15819	psbK	Photosystem II reaction center protein K (PSII-K)	1	45
Q55354	psbL	Photosystem II reaction center protein L (PSII-L)	1	39
P72701	psbM	Photosystem II reaction center protein M (PSII-M)	1	35
P26286	psbN	Protein PsbN	1	43
P10549	psbO	Photosystem II manganese-stabilizing polypeptide (MSP)	1	274
P74787	psbT	Photosystem II reaction center protein T (PSII-T)	1	31
Q55332	psbU	Photosystem II 12 kDa extrinsic protein (PS II complex 12 kDa extrinsic protein) (PSII-U)	1	131
Q55013	psbV	Cytochrome c-550 (Cytochrome c549) (Cytochrome c550) (Low-potential cytochrome c)	1	160
P72575	psbX	Photosystem II reaction center X protein	1	39
P73676	psbY	Photosystem II protein Y	1	39
P73528	psbZ	Photosystem II reaction center protein Z (PSII-Z)	1	62
Q55438	ycf12	Photosystem II reaction center protein Ycf12	1	39
Total				3488

Table T7: Cytochrome b$_6$f homodimer, plastocyanin and FNR in *Synechocystis* 6803.

Uniprot ID	Gene name	Protein name	Stoichiometry	Length
P26287	petA	Cytochrome f	2	328
Q57038	petB	Cytochrome b6	2	222
P74714	petC1	Cytochrome b6-f complex iron-sulfur subunit 1 (Rieske iron-sulfur protein 1)	2	178
P27589	petD	Cytochrome b6-f complex subunit 4	2	160
P74149	petG	Cytochrome b6-f complex subunit 5	2	38
P74810	petM	Cytochrome b6-f complex subunit 7	2	36
P72717	petN	Cytochrome b6-f complex subunit 8	2	29
Total				1982
P21697	petE	Plastocyanin	1	126
Q55318	petH	Ferredoxin–NADP reductase (FNR)	1	413

Table T8: ATP-synthase in *Synechocystis* 6803.

Uniprot ID	Gene name	Protein name	Stoichiometry	Length
P27179	atpA	ATP synthase subunit alpha (ATP synthase F1 sector subunit alpha)	3	503
P27178	atpB	ATP synthase subunit a (ATP synthase F0 sector subunit a)	1	276
P26533	atpC	ATP synthase epsilon chain (ATP synthase F1 sector epsilon subunit)	1	136
P26527	atpD	ATP synthase subunit beta (ATP synthase F1 sector subunit beta)	3	483
P27182	atpE	ATP synthase subunit c (ATP synthase F(0) sector subunit c)	10-14	81
P27181	atpF	ATP synthase subunit b (ATP synthase F(0) sector subunit b)	1	179
P17253	atpG	ATP synthase gamma chain (ATP synthase F1 sector gamma subunit)	1	314
P27183	atpG	ATP synthase subunit b' (ATP synthase F(0) sector subunit b')	1	143
P27180	atpH	ATP synthase subunit delta (ATP synthase F(1) sector subunit delta)	1	185
On average				5163

Table T9: Phycobilisome in *Synechocystis* 6803.

Uniprot ID	Gene name	Protein name	Stoichiometry	Length
		3-cylindric core each with 4 trimeric allophycocyanin $(\alpha\beta)_3$ discs		
Q01951	apcA	Allophycocyanin alpha chain	34	161
Q01952	apcB	Allophycocyanin beta chain	34	161
Q01950	apcC	Phycobilisome linker polypeptide, allophycocyanin-associated, core (LC 7.8)	6	67
P72870	apcD	Allophycocyanin subunit alpha-B	2	161
Q55544	apcE	Phycobiliprotein ApcE (Phycobilisome LCM core-membrane linker polypeptide)	6	896
P74551	apcF	Allophycocyanin subunit beta-18	2	169
		6 rods each with 3 hexameric phycocyanin $(\alpha\beta)_6$ discs		
Q54715	cpcA	C-phycocyanin alpha chain	108	162
Q54714	cpcB	C-phycocyanin beta chain	108	172
P73203	cpcC1	Phycobilisome linker polypeptide, phycocyanin-associated, rod 1	6	291
P73204	cpcC2	Phycobilisome linker polypeptide, phycocyanin-associated, rod 2	6	273
P73202	cpcD	Phycobilisome linker polypeptide, phycocyanin-associated, rod (L-8.9/R) (Rod-capping linker protein)	6	83
P74625	cpcG	Phycobilisome rod-core linker polypeptide CpcG	6	249
Total				58834

References

[1] Douwe Molenaar, Rogier van Berlo, Dick de Ridder, and Bas Teusink. Shifts in growth strategies reflect tradeoffs in cellular economics. *Mol. Syst. Biol.*, 5:323, 2009.

[2] Arijit Maitra and Ken A Dill. Bacterial growth laws reflect the evolutionary importance of energy efficiency. *Proc. Natl. Acad. Sci. U.S.A.*, 112(2):406–411, 2015.

[3] Bo-Ping Han. Photosynthesis–irradiance response at physiological level: a mechanistic model. *J. Theor. Biol.*, 213(2):121–127, 2001.

[4] Bo-Ping Han. A mechanistic model of algal photoinhibition induced by photodamage to photosystem-ii. *J. Theor. Biol.*, 214(4):519–527, 2002.

[5] Hans Bremer and Patrick P Dennis. Modulation of chemical composition and other parameters of the cell at different exponential growth rates. *EcoSal Plus*, 3(1), 2008.

[6] Andrea Y. Weiße, Diego A. Oyarzún, Vincent Danos, and Peter S. Swain. Mechanistic links between cellular trade-offs, gene expression, and growth. *Proc. Natl. Acad. Sci. U.S.A.*, 112(9):E1038–47, 2015.

[7] Henning Knoop, Marianne Gründel, Yvonne Zilliges, Robert Lehmann, Sabrina Hoffmann, Wolfgang Lockau, and Ralf Steuer. Flux balance analysis of cyanobacterial metabolism: The metabolic network of Synechocystis sp. PCC 6803. *PLoS Comput. Biol.*, 9(6):e1003081, 2013.

[8] UniProt Consortium. UniProt: the universal protein knowledgebase. *Nucleic Acids Res.*, 45(D1):D158–D169, 2017.

[9] Alap Raman Subramanian. Copies of proteins L7 and L12 and heterogeneity of the large subunit of Escherichia coli ribosome. *J. Mol. Biol.*, 95(1):1–4, 1975.

[10] Wim FJ Vermaas. Photosynthesis and respiration in cyanobacteria. *eLS*, 2001.

[11] Ana A Arteni, Ghada Ajlani, and Egbert J Boekema. Structural organisation of phycobilisomes from synechocystis sp. strain PCC6803 and their interaction with the membrane. *Biochim. Biophys. Acta*, 1787(4):272–279, 2009.

[12] Hisako Kubota, Isamu Sakurai, Kenta Katayama, Naoki Mizusawa, Shunsuke Ohashi, Masami Kobayashi, Pengpeng Zhang, Eva-Mari Aro, and Hajime Wada. Purification and characterization of photosystem i complex from Synechocystis sp. PCC 6803 by expressing histidine-tagged subunits. *Biochim. Biophys. Acta, Bioenerg.*, 1797(1):98–105, 2010.

[13] Alexandra-M. Reimers, Henning Knoop, Alexander Bockmayr, and Ralf Steuer. Cellular trade-offs and optimal resource allocation during cyanobacterial diurnal growth. *Proc. Natl. Acad. Sci. U.S.A.*, 114(31):E6457–E6465, 2017.

[14] Ron Milo and Rob Phillips. *Cell biology by the numbers*. Taylor & Francis Ltd., 2015.

[15] Niall M Mangan and Michael P Brenner. Systems analysis of the CO2 concentrating mechanism in cyanobacteria. *eLife*, 3:e02043, 2014.

[16] Elena V Kupriyanova, Maria A Sinetova, Sung Mi Cho, Youn-Il Park, Dmitry A Los, and Natalia A Pronina. CO2-concentrating mechanism in cyanobacterial photosynthesis: organization, physiological role, and evolutionary origin. *Photosynth. Res.*, 117(1):133–146, 2013.

[17] Brian M Hopkinson, Jodi N Young, Anna L Tansik, and Brian J Binder. The minimal CO2-concentrating mechanism of Prochlorococcus spp. MED4 is effective and efficient. *Plant Physiol.*, 166(4):2205–2217, December 2014.

[18] Bo-Ping Han, Markku Virtanen, Jorma Koponen, and Milan Straskraba. Effect of photoinhibition on algal photosynthesis: a dynamic model. *J. Plankton Res.*, 22(5):865–885, 2000.